

Multimode Coupling and Nonlinear-Gain Effects in Distributed and Helical Feedback Gas Lasers

J. Arnesson, Cui Dafu*, S. Gnepf, and F. K. Kneubühl

Institute of Quantum Electronics, ETH, CH-8093 Zürich, Switzerland

Received 18 November 1988/Accepted 15 February 1989

Abstract. We present a detailed experimental and theoretical study on the waveguide modes of distributed feedback (DFB) and helical feedback (HFB) gas lasers including for the first time the experimental verification of multimode-coupling and nonlinear-gain phenomena. For this purpose we used oversized hollow metal waveguides with periodic or helical corrugations. The latter exhibit the symmetry of either the single helix or the double helix. For the interpretation of our observations we developed a coupled-wave theory extended to multi-mode coupling and adapted the nonlinear-gain approach for strong coupling by Haus. The experiments with DFB and HFB gas lasers give new relevant information on these phenomena.

PACS: 42.55E, 42.60

Distributed feedback was introduced in the early 1970s [1, 2] in dye lasers. In one of the systems [2], the dye was pumped with the frequency-doubled radiation of a ruby laser. The coherent pump radiation was first split in two and then superimposed in the dye cell to form a periodic interference pattern. Thus, the laser dye was pumped periodically along a specific axis. The result was laser action without resonator mirrors providing the optical feedback. This feedback was obtained by quasi-Bragg reflection on the axially periodic gain modulation of the laser dye. Since in this arrangement, the optical feedback was not localized at the mirror surfaces, but distributed along the laser medium, it was named distributed feedback or DFB. This DFB incorporated in the dye laser resulted in an extremely narrow and intense stimulated emission. In order to understand this phenomenon Kogelnik and Shank [3] performed a coupled-wave theory on the laser modes of a bulk medium with weak axially periodic modulation of refractive index and/or gain. They demonstrated that the threshold gains of the longitudinal DFB laser modes show a minimum near the Bragg frequency which provides an effective longitudinal mode selection in laser media with broadband gain.

However, their coupled-wave theory [3] does not properly explain the narrow emission of the first DFB dye laser [4] by almost pure gain modulation. The high selectivity among the longitudinal modes demonstrated for DFB dye lasers stimulated intensive research in this field. As a consequence, the first DFB semiconductor laser was realized by Nakamura et al. [5] and, almost simultaneously, the concept of a DFB gas laser was devised by Marcuse [6]. Seven years passed before DFB was incorporated in a gas laser [7–10], shortly after the application of a distributed Bragg reflector (DBR) to an optical gas laser [11]. The first DFB in a gas laser was achieved with an optically pumped $496\ \mu\text{m}$ CH_3F laser with an axially periodic waveguide of rectangular cross section. The observed mode configuration was explained by coupled-wave theory for periodic index modulation. In subsequent studies Preiswerk et al. [12–14] observed the first resonant emission of a laser of pure helical symmetry. This laser was an optically pumped $496\ \mu\text{m}$ CH_3F laser similar to the first DFB gas laser, yet equipped with a hollow metal waveguide of helical symmetry instead of a hollow axially periodic metal waveguide. On the basis of group theoretical considerations, the helical feedback (HFB) of the radiation of this laser was explained as a quasi-Bragg effect similar, yet different from standard DFB [12–14]. The observation of only

* On leave from Academia Sinica, Beijing, People's Republic of China

one resonant emission of the HFB gas laser in comparison to that of the numerous resonances of the corresponding DFB gas laser demonstrated the advantage of HFB over DFB with respect to mode selectivity due to polarization and symmetry effects. However, it was of basic interest to find resonant HFB emissions in addition to the resonance already observed [14], because they give information on the detailed mode configurations of HFB lasers.

As mentioned above, the present DFB and HFB gas lasers are operated with periodic or helical modulation of the waveguide cross section which is similar to most DFB semiconductor lasers with periodic modulated thickness of the active layer (e.g. [15–25]). In theory, however, all these types of lasers can be characterized by a periodic or helical modulation of the refractive index of the bulk of the laser medium [3]. On the contrary, gain modulation dominates in today's DFB dye lasers (e.g. [26–33]). The DFB semiconductor lasers are of practical significance with respect to optical communication and integrated optics. Unfortunately, they are not well suited for the test of theories (e.g. [3, 4, 18–20, 34, 35]) on DFB with periodic modulation of refractive index, since the detailed experimental study of their mode structure encounters serious problems, e.g. with tuning. This is manifested by the relatively modest results [15–17, 21–25] even under good experimental conditions. In contrast, the DFB gas lasers permit to test experimentally the theories on DFB with periodic modulation of effective refractive index in great detail (e.g. [9, 13, 14, 36]) because they can be tuned conveniently and, in addition, exhibit a narrow gain width. This is the main reason for their investigation. The results from their study are therefore of interest to laser theoreticians as well as to designers of DFB semiconductor lasers.

The purpose of the study on DFB and HFB gas lasers reported in this paper was firstly to detect the additional HFB resonant emissions mentioned above and, secondly, to gain insight into the origin and configuration of HFB modes as well as their relation to the standard DFB modes. By an intensified search, we were able to observe the missing additional HFB modes early in this project [37–38]. Subsequently, we investigated experimentally as well as theoretically the modes of 496 μm CH_3F laser with hollow metal waveguides of three different symmetries which were defined in a previous paper [14]. These were, besides of the symmetry G_{hs} of the symmetric helix inherent to the waveguide used for the original HFB gas laser [12–14], the symmetry $G_{2\text{hs}}$ of the symmetric double-helix and the symmetric G_{ps} of the circular cylinder with symmetric axially periodic corrugation. The latter provides DFB which can be compared with the HFB due to the waveguides of the symmetries G_{hs} and $G_{2\text{hs}}$. An

optical waveguide of the effective symmetry $G_{2\text{hs}}$ was previously applied in the form of a cholesteric liquid crystal in a dye laser which was originally labelled DFB laser [39] and later recognized as an HFB laser [34, 40]. Therefore, it was of interest to realize and study an HFB gas laser with a waveguide of the symmetry $G_{2\text{hs}}$ of the double-helix.

Group theory is a valuable tool for evaluating the general characteristics of DFB and HFB lasers, the symmetries of the fields of the modes as well as of the existence of couplings between these modes. Unfortunately, it does not give information on the strength of fields and couplings. For hollow metal waveguides with the corrugations required for DFB and HFB lasers, this information can be obtained by various methods studied in the past [41–48]. The only method, however, which allows the inclusion of helical corrugations is the theory outlined by Katsenelenbaum [41]. It is quite general yet requires detailed work if applied.

In Sect. 1, we present the perturbation theory on corrugated hollow metal waveguides for DFB and HFB lasers on the basis of an extension of Katsenelenbaum's approach. This extension improves the applicability of this approach and allows for waveguide modes represented by complex fields. Throughout Sect. 1, we apply the general multi-mode formalism referring to the simplified two-mode coupling theory. Finally, we also discuss the influence of nonlinear gain saturation in addition to the standard linear coupled-wave theory. Nonlinear gain saturation is relevant for strong DFB and HFB mode couplings because of their strong internal fields.

Section 2 of this paper is devoted to experiments performed with optically pumped 496 μm CH_3F lasers equipped with hollow metal waveguides of the symmetries G_{ps} , G_{hs} , and $G_{2\text{hs}}$ which provide DFB and HFB. Firstly, we discuss the waveguide design, the tuning mechanism, and the experimental set-up. Secondly, we present the observed DFB and HFB modes of the three different types of waveguides and the interpretation of these modes based on the theory outlined in Sect. 1. The results presented include the first demonstration of the effect of nonlinear gain saturation on the intensity distribution of DFB and HFB modes.

1. Theory of DFB and HFB Gas Lasers with Corrugated Hollow Metal Laser Waveguides

The aim of this section is to introduce a perturbation theory suitable for the calculation of DFB and HFB laser resonances. In the first Sect. 1.1, we derive the complex modes of a smooth metal waveguide and present an ortho-normalization condition which, due to the definition of the backward running modes,

allows for orthogonal counterpropagating waveguide modes. In Sect. 1.2, we formally introduce a magnetic surface current to describe a waveguide perturbation. With this formalism and with an expanded form of the waveguide modes, we derive an integral relation for the amplitude factors of the single modes. From this relation and the magnetic surface current appropriate for a hollow metallic waveguide with weak wall perturbation derived in Sect. 1.3, we deduce an expression for the coupling coefficients between various coupling modes. In Sect. 1.4, we concentrate on the waveguides with axially periodic and helical perturbations. Firstly, we formulate the generalized coupled-mode equation valid for multi-mode couplings together with its formal solution for harmonic perturbations of various chiralities. This includes the solution of the simplified two-mode coupling. Secondly, we apply the wave potential and the expression for the coupling coefficients derived in Sect. 1.3 to the evaluation of the coupling constants and the selection rule for different types of pair-couplings. In Sect. 1.5, we present a modified dispersion relation valid for two-mode couplings and derived under consideration of our experimental conditions (cf. Sect. 2). Section 1.6 is devoted to the resonance condition for the extended mode coupling. Besides the evaluation of the pure resonance condition, we also derive an alternative method for the calculation of the resonant perturbation periods or pitches together with their corresponding threshold gains. This method devised for multi-mode coupling is based on the transmission or reflection matrix of the waveguide structure. Subsequently, we discuss the reduction of this formalism to two-mode coupling. In Sect. 1.7, we consider the attenuation of waveguide modes in the FIR at 496.1 μm wavelength which corresponds to the strongest emission line of CH_3F used in our experiments. The last Sect. 1.8 of this chapter is devoted to the nonlinear saturation of the laser medium and its effect on the relative output power of different longitudinal DFB and HFB modes.

1.1. Modes of a Cylindric Hollow Metal Waveguide

The modes of a hollow cylindrical metal waveguide without wall corrugation can be derived from a scalar wave potential $u(\mathbf{r}, t)$ corresponding to the electric and magnetic Hertz vectors for TE and TM modes respectively [49]. Assuming harmonic time dependent electromagnetic fields of the form

$$\mathbf{E}(\mathbf{r}, t) = \text{Re}\{\mathbf{E}(\mathbf{r})e^{i\omega t}\}, \quad \mathbf{H}(\mathbf{r}, t) = \text{Re}\{\mathbf{H}(\mathbf{r})e^{i\omega t}\}, \quad (1)$$

we define the scalar wave potential

$$u(\mathbf{r}, t) = u(\mathbf{r})e^{i\omega t} \quad (2)$$

with

$$u(\mathbf{r}) = \begin{cases} \Phi(\mathbf{r}_t)e^{-i\beta z} & \text{for TM modes} \\ \Psi(\mathbf{r}_t)e^{-i\beta z} & \text{for TE modes} \end{cases} \quad (3)$$

Here we have chosen the wave propagation parallel to z . ω denotes the circular frequency, β the propagation constant, \mathbf{r} the space coordinate vector, and \mathbf{r}_t its component perpendicular to the direction of propagation. With the potentials (3), we find in accordance with Borgnis and Papas [49] for the electromagnetic field of the waveguide modes

$$\begin{aligned} \mathbf{E}(\mathbf{r}) &= -i\beta\nabla_t u(\mathbf{r}) + k_c^2 u(\mathbf{r})\mathbf{e}_z \\ \mathbf{H}(\mathbf{r}) &= -ikZ_0^{-1}\mathbf{e}_z \times \nabla_t u(\mathbf{r}) \end{aligned} \quad \text{for TM modes} \quad (4)$$

and

$$\begin{aligned} \mathbf{E}(\mathbf{r}) &= ikZ_0\mathbf{e}_z \times \nabla_t u(\mathbf{r}) \\ \mathbf{H}(\mathbf{r}) &= -i\beta\nabla_t u(\mathbf{r}) + k_c^2 u(\mathbf{r})\mathbf{e}_z \end{aligned} \quad \text{for TE modes} \quad (5)$$

with ∇_t indicating the transverse component of the vector gradient. Z_0 is the vacuum impedance, $k = 2\pi/\lambda$ the free-space circular wavenumber, and k_c the mode-characteristic cut-off circular wavenumber. For a waveguide with ideally conducting walls, the latter is derived from the eigenvalue problem

$$\Delta_t u(\mathbf{r}) + k_c^2 u(\mathbf{r}) = 0 \quad (6)$$

with the appropriate boundary conditions

$$u(\mathbf{r}) = 0 \quad \text{for TM modes} \quad (7)$$

$$\frac{\partial u(\mathbf{r})}{\partial n} = 0 \quad \text{for TE modes.}$$

Δ_t is the transverse part of the Laplacian and n denotes the direction perpendicular to the boundary.

By introduction of (6) into the Helmholtz equation

$$\Delta u(\mathbf{r}) + k^2 u(\mathbf{r}) = 0 \quad (8)$$

and by consideration of the scalar wave potential (3), we find the dispersion relation for waveguide modes

$$\beta^2 = k^2 - k_c^2. \quad (9)$$

In order to avoid ambiguities and to be consistent with previous group theoretical investigations [14], we consider backward running modes as time-reversed forward propagating modes. Consequently, we derive the backward propagating modes from the modes defined by (3)–(9) and $\beta > 0$ by application of the time-reversal operator T , which implies

$$Tu(\mathbf{r}) = u(\mathbf{r})^*. \quad (10)$$

Thus, we obtain the following field transformations

$$\begin{aligned} \mathbf{TE} &= \mathbf{E}^*, \quad \mathbf{TH} = -\mathbf{H}^* \quad \text{for TM modes} \\ \mathbf{TE} &= -\mathbf{E}^*, \quad \mathbf{TH} = \mathbf{H}^* \quad \text{for TE modes} \end{aligned} \quad (11)$$

with the asterisk indicating the complex conjugate.

In analogy to the condition of orthonormalization used by Katsenelenbaum [41], which holds for the field amplitudes \mathbf{E} and \mathbf{H} of the waveguide modes labelled by p and q , we put

$$\int_A (\mathbf{E}_p \times \mathbf{H}_q^* + \mathbf{E}_q^* \times \mathbf{H}_p) \cdot \mathbf{e}_z dA = 4 \operatorname{sgn}(\beta_p) \delta_{pq}, \quad (12)$$

where the integration is extended over the cross section A of the waveguide perpendicular to the axial unit vector \mathbf{e}_z . δ_{pq} denotes the Kronecker delta and $\operatorname{sgn}(x)$ the sign function. β is positive for a forward running and negative for a backward running wave. By definition (12), the average power carried by a mode running through the waveguide cross section is normalized to $+1$ W for a forward propagating mode and -1 W for a mode in the reverse direction. Definition (12) is equivalent to definitions by other authors [49–51], yet it has the advantage that TE and TM modes as well as, due to (11), a forward propagating mode and the corresponding time-reversed backward propagating mode are orthogonal. This in contrast to the theory by Katsenelenbaum [41], where the orthogonality condition is tied to the definition of the backward propagating modes.

1.2. Perturbation of Waveguide Modes by Electric and Magnetic Current Densities

The electric and magnetic fields \mathbf{E} and \mathbf{H} in vacuum in the presence of an electric current density \mathbf{j}^e and, formally, a magnetic current density \mathbf{j}^m , obey the extended Maxwell equations [52]

$$\nabla \times \mathbf{E} = -ikZ_0 \mathbf{H} - \mathbf{j}^m, \quad (13a)$$

$$\nabla \times \mathbf{H} = ikZ_0^{-1} \mathbf{E} + \mathbf{j}^e, \quad (13b)$$

$$\nabla \cdot \mathbf{E} = 0, \quad (13c)$$

$$\nabla \cdot \mathbf{H} = 0. \quad (13d)$$

We now consider two sets $k=1, 2$ of fields \mathbf{E}_k , \mathbf{H}_k and current densities \mathbf{j}_k^e , \mathbf{j}_k^m in a volume V enclosed by the surface F , and form the scalar products of (13a) and (13b) for set 1 with \mathbf{H}_2^* and \mathbf{E}_2^* as well as the corresponding products of the complex conjugates of (13a) and (13b) for set 2 with \mathbf{H}_1 and \mathbf{E}_1 . Subsequently, we apply the vector identity

$$\nabla \cdot (\mathbf{a} \times \mathbf{b}) = \mathbf{b} \cdot (\nabla \times \mathbf{a}) - \mathbf{a} \cdot (\nabla \times \mathbf{b}). \quad (14)$$

By addition and application of the Gauss divergence theorem, we find

$$\int_F (\mathbf{E}_1 \times \mathbf{H}_2^* + \mathbf{E}_2^* \times \mathbf{H}_1) \cdot \mathbf{n} dF = - \int_V (\mathbf{j}_1^e \cdot \mathbf{E}_2^* + \mathbf{j}_2^{e*} \cdot \mathbf{E}_1 + \mathbf{j}_1^m \cdot \mathbf{H}_2^* + \mathbf{j}_2^{m*} \cdot \mathbf{H}_1) dV. \quad (15)$$

This relation is analogous to that of Vainshtein [52] with the difference that it contains complex conjugate quantities.

For the calculations described in the following Sect. 1.3, we need to adapt (15) to the description of a hollow cylindrical waveguide with an ideally conducting wall and a wall perturbation represented by a magnetic surface-current density \mathbf{i}^m on the wall.

In the unperturbed waveguide with $\mathbf{i}^m=0$, the modes with the fields \mathbf{E}_p , \mathbf{H}_p are those derived in the previous Sect. 1.1. In the presence of a perturbation with $\mathbf{i}^m \neq 0$, we expand the fields in modes of the unperturbed waveguide [42, 52]

$$\mathbf{E} = \sum_p c_p(z) \mathbf{E}_p, \quad \mathbf{H} = \sum_p c_p(z) \mathbf{H}_p. \quad (16)$$

In order to apply (15) to the study of perturbed waveguides, we identify \mathbf{E}_1 , \mathbf{H}_1 of (15) with \mathbf{E} , \mathbf{H} of (16) as well as \mathbf{E}_2 , \mathbf{H}_2 with \mathbf{E}_p , \mathbf{H}_p . In the absence of external current densities, we can assume

$$\mathbf{j}_1^e = \mathbf{j}_2^e = \mathbf{j}_2^m = 0, \quad (17)$$

$$\mathbf{j}_1^m = \begin{cases} \mathbf{i}^m & \text{on the wall} \\ 0 & \text{elsewhere} \end{cases}.$$

We now choose as closed surface in (15), the surface formed by two planes perpendicular to the z -axis of the waveguide and situated at z and $z+dz$ plus the waveguide wall between these two planes. Taking into account the condition (12) of orthonormalization and the fact that \mathbf{i}^m indicates a pure surface-current density, we can derive the following relation [42] from (15)

$$\frac{dc_p(z)}{dz} = - \frac{1}{4 \operatorname{sgn}(\beta_p)} \oint_{s(z)} \mathbf{i}^m \cdot \mathbf{H}_p^* ds. \quad (18)$$

The integral is performed over the closed path $s(z)$ corresponding to the inner cross section of the unperturbed waveguide at the axial position z .

1.3. Surface Perturbations of Cylindric Hollow Metal Waveguides

We consider a hollow metal waveguide with a small wall perturbation as shown in Fig. 1. The inner wall S

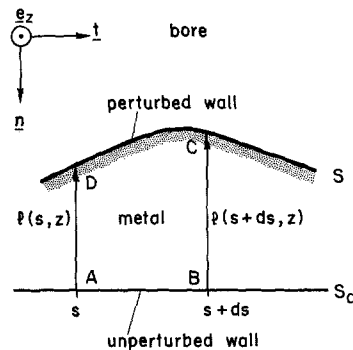


Fig. 1. Boundary perturbation S of a hollow cylindrical waveguide

of the perturbed waveguide is at a distance $l(s, z)$ from the wall S_0 of the unperturbed waveguide. z indicates the axial coordinate and s the path on the circumference of the unperturbed wall at z . The distance l is measured perpendicular to the unperturbed wall S_0 and is positive when S is inside S_0 in agreement with Katsenelenbaum [41]. \mathbf{n} and \mathbf{t} denote unit vectors in perpendicular and tangential direction to the unperturbed wall S_0 . Together with the axial unit vector \mathbf{e}_z , the vector triple $(\mathbf{n}, \mathbf{t}, \mathbf{e}_z)$ forms a right-handed triad

$$\mathbf{n} \times \mathbf{t} = \mathbf{e}_z. \quad (19)$$

We now apply Stokes' theorem to (13a) with $\mathbf{j}^m = 0$ for an infinitesimal area $ABCD$ of width ds with the assumption that $|l|$ is considerably smaller than the wavelength and the waveguide cross section. Thus, the boundary condition on the ideally conducting perturbed wall S can be replaced to the first order of l by an equivalent boundary condition on S_0 [41]

$$\mathbf{E} \cdot \mathbf{t} = ikZ_0 l \mathbf{t} \cdot (\mathbf{n} \times \mathbf{H}) + \mathbf{t} \cdot \nabla(l\mathbf{E} \cdot \mathbf{n}). \quad (20)$$

\mathbf{E} as well as \mathbf{H} are evaluated on the unperturbed surface S_0 .

In analogy to the relation between electric surface currents and magnetic fields on the surface, the tangential electric field component ($\mathbf{E} \cdot \mathbf{t}$) on the unperturbed wall S_0 corresponds to a magnetic surface current on S_0 given by

$$\mathbf{i}^m = \mathbf{i}_H^m + \mathbf{i}_E^m, \quad (21)$$

where

$$\mathbf{i}_H^m = ikZ_0 l \mathbf{n} \times (\mathbf{n} \times \mathbf{H}), \quad (22a)$$

$$\mathbf{i}_E^m = \mathbf{n} \times \nabla(l\mathbf{E} \cdot \mathbf{n}). \quad (22b)$$

If (21) is combined with (18), the resulting integral is split in two parts according to (22). Making use of (13b) and of some transformations, we can represent these two parts as follows

$$- \oint_{s(z)} \mathbf{i}_H^m \cdot \mathbf{H}_p^* ds = ikZ_0 \oint_{s(z)} l \{ (\mathbf{H} \cdot \mathbf{t})(\mathbf{H}_p^* \cdot \mathbf{t}) + (\mathbf{H} \cdot \mathbf{e}_z)(\mathbf{H}_p^* \cdot \mathbf{e}_z) \} ds, \quad (23a)$$

$$- \oint_{s(z)} \mathbf{i}_E^m \cdot \mathbf{H}_p^* ds = -ikZ_0^{-1} \oint_{s(z)} l (\mathbf{E} \cdot \mathbf{n})(\mathbf{E}_p^* \cdot \mathbf{n}) ds - \frac{\partial}{\partial z} \oint_{s(z)} l (\mathbf{E} \cdot \mathbf{n})(\mathbf{H}_p^* \cdot \mathbf{t}) ds. \quad (23b)$$

An explicit evaluation with the aid of (4), (5), and (16) shows that the second term of (23b) can be neglected [42]. The remaining terms of (23) result in the following system of ordinary differential equations for the mode coefficients defined by (16) and (18)

$$\frac{dc_p}{dz} = \sum_q F_{pq}(z)c_q(z) \quad (24)$$

with

$$F_{pq}(z) = \frac{ik}{4Z_0 \operatorname{sgn}(\beta_p)} \times \oint_{s(z)} l \{ Z_0^2 (H_{ps}^* H_{qs} + H_{pz}^* H_{qz}) - E_{pn}^* E_{qn} \} ds \quad (25)$$

and

$$H_{js} = \mathbf{H}_j \cdot \mathbf{t}, \quad H_{jz} = \mathbf{H}_j \cdot \mathbf{e}_z \quad (26)$$

$$E_{jn} = \mathbf{E}_j \cdot \mathbf{n}; \quad j = p, q.$$

The matrix elements $F_{pq}(z)$ depend on the definition of the scalar wave potentials u_p and u_q . If they are replaced by $\tilde{u}_p = r_p u_p$, $\tilde{u}_q = r_q u_q$ with r_p, r_q as arbitrary complex constants, the matrix elements $F_{pq}(z)$ are replaced by

$$\tilde{F}_{pq}(z) = \frac{r_q}{r_p} F_{pq}(z). \quad (27)$$

This follows from (25) and the condition (12) of orthonormalization. Furthermore, the matrix elements $F_{pq}(z)$ obey the symmetry relation

$$\operatorname{sgn}(\beta_q) F_{qp}(z) + \operatorname{sgn}(\beta_p) F_{pq}^*(z) = 0. \quad (28)$$

This relation is equivalent to the condition, that the total power carried in the positive z -direction of the lossless waveguide

$$\bar{P}(z) = \sum_p \operatorname{sgn}(\beta_p) c_p(z) c_p^*(z) = \bar{P} \quad (29)$$

does not depend on z .

Here, it should be noticed that the expressions for the coupling coefficients inherent to a cylindrical deformed metal waveguide as derived by Joindot [45] is equivalent to the relations (24) and (25). This can be demonstrated by transformations. The difference of formulation is due to the different definition of the waveguide modes.

1.4. Solution of the Coupled-Wave Equation for Waveguides with Axially Periodic or Helical Perturbations

In the following, we restrict our considerations to axially periodic and helical perturbations of a cylindrical waveguide of circular cross section. We assume a harmonic perturbation of the form

$$l(\phi, z) = a_1 \cos[\bar{m}\phi - 2\beta_0 z], \quad (30)$$

$$\phi = \arctan(y/x); \quad \bar{m} = 0, \pm 1, \pm 2, \pm 3, \dots,$$

where $\beta_0 = \pi/L$ denotes the Bragg circular wavenumber and \bar{m} is a measure for the chirality of the perturbation. L indicates the period or the pitch of the

Table 1. Symmetries of considered perturbations denoted according to Preiswerk et al. [13]

$ \bar{m} $	Symmetry	Period	Pitch
0	G_{ps} symmetric periodic circular structure	L	–
1	G_{hs} symmetric single-helix	–	L
2	G_{2hs} symmetric double-helix	L	$2L$

perturbation. Axially periodic perturbations are characterized by $\bar{m}=0$, right-handed and left-handed helical perturbations by $\bar{m}>0$ and $\bar{m}<0$ respectively.

The symmetries of the perturbations represented by (30) can be evaluated with the group theory of waveguides and laser structures developed by Preiswerk et al. [14]. For $|\bar{m}| \leq 2$, the result is given in Table 1.

For the circular cylindrical metal waveguide with the perturbation $l(\phi, z)$ defined by (30), we now consider the case of m forward running modes with coefficients $c_{+p}(z)$ coupling to n backward running modes with coefficients $c_{-q}(z)$ near the Bragg condition, where the detuning or mismatch is given by

$$2\Delta_{+p-q} = -2\Delta_{-q+p} = \beta_{+p} - \beta_{-q} - 2\beta_0 \simeq 0. \quad (31)$$

If we neglect terms with large exponentials in (25) in accordance with the rotating-wave approximation common in laser physics [53], we find for the functions F_{+p-q} which determine the coupling coefficients by (24)

$$F_{+p-q} = f_{+p-q} e^{i2\Delta_{+p-q}z}. \quad (32)$$

f_{+p-q} are complex constants depending on the modes $+p$ and $-q$. The symmetry condition (28) is now

$$F_{-q+p} = F_{+p-q}^*. \quad (33)$$

The exponential dependence in (32) can be removed by the transformation

$$c_{+p} = A_{+p} e^{i\Delta_{+p}z}; \quad c_{-q} = A_{-q} e^{i\Delta_{-q}z}, \quad (34)$$

where

$$\Delta_{+p} = \beta_{+p} - \beta_0; \quad \Delta_{-q} = \beta_{-q} + \beta_0. \quad (35)$$

If we now introduce (31), (32), (34), and (35) in (24), we find the following system of $(m+n)$ ordinary differential equations with constant coefficients for A_{+p} and A_{-q}

$$\begin{aligned} \frac{dA_{+p}}{dz} + i\Delta_{+p}A_{+p} &= \sum_q f_{+p-q} A_{-q}, \\ \frac{dA_{-q}}{dz} + i\Delta_{-q}A_{-q} &= \sum_p f_{-q+p} A_{+p}. \end{aligned} \quad (36)$$

In addition, we can introduce loss or gain in the waveguide by replacing Δ_{+p} by $\Delta_{+p} + i\alpha_{+p}$ and Δ_{-q} by $\Delta_{-q} - i\alpha_{-q}$ with $\alpha > 0$ for gain and $\alpha < 0$ for loss. Equation (36) is solved by the eigenfunctions [54]

$$A_{+pj} = s_{+pj} e^{-i\eta_j z}; \quad A_{-qj} = s_{-qj} e^{-i\eta_j z} \quad (37)$$

with

$$j = 1, 2, 3, \dots, m+n$$

which can be derived from the solution of the eigenvalue problem

$$\mathbf{K} \mathbf{s}_j = -i\eta_j \mathbf{s}_j; \quad j = 1, 2, 3, \dots, m+n, \quad (38)$$

where $-i\eta_j$ and \mathbf{s}_j are the eigenvalues and the eigenvectors of the $(m+n) \times (m+n)$ coupling matrix \mathbf{K} given by (36). Provided that the eigenvalues $-i\eta_j$ are discrete, the general solution can be written as

$$\mathbf{A}(z) = \sum a_j \mathbf{A}_j = \sum a_j \mathbf{s}_j e^{-i\eta_j z}. \quad (39)$$

The vector $\mathbf{A}(z)$ contains all $(m+n)$ functions A_{+p} and A_{-q} . a_j are arbitrary constants. In general, the eigenvalue problem represented by (38) has to be solved numerically. However, a simple analytical solution is possible in the case of two-mode coupling. This is a good approximation if the detunings $|\Delta_{+p-q}|$ and $|\Delta_{-p+q}|$ versus other modes are considerably larger than the respective coupling coefficients $|f_{+p-q}|$ and $|f_{-q+p}|$ [46].

In the following considerations on the two-mode coupling, we denote the coefficients of the forward and backward running modes by c_+ and c_- and the coupling coefficients by

$$\begin{aligned} f_{+-} &= i\kappa_- = i\kappa e^{-ix}, \\ f_{-+} &= -i\kappa_+ = -i\kappa e^{+ix}. \end{aligned} \quad (40)$$

Equation (40) is in agreement with (32) and (33). By applying the transformation

$$c_{\pm} = A_{\pm} e^{\pm iAz} \quad (41)$$

with

$$2\Delta = \beta_+ - \beta_- - 2\beta_0 = \beta_+ - \beta_- - 2\pi/L \quad (42)$$

we obtain from (24) by taking into account gain or loss α_{\pm}

$$\frac{dA_+}{dz} = -i(\Delta + i\alpha_+)A_+ + i\kappa_- A_-, \quad (43a)$$

$$\frac{dA_-}{dz} = -i\kappa_+ A_+ + i(\Delta + i\alpha_-)A_-. \quad (43b)$$

These equations correspond to the coupling equations given by other authors [42, 46, 47] as well as those originally derived by Kogelnik and Shank [3] for the description of DFB lasers with a bulk laser medium

with periodic index and/or gain modulation. Recently, they were also used in a slightly modified form to describe the resonances of a phase-matched grazing-incidence DFB gas laser [36]. Similar equations were derived [43,44] for two-mode couplings in circular and parallel-plate waveguides with sinusoidally corrugated walls.

The solution of (43) in the form (40) is given by

$$\begin{pmatrix} A_+(z) \\ A_-(z) \end{pmatrix} = a_+ \begin{pmatrix} 1 \\ s_1 \end{pmatrix} e^{(\alpha_+ - i\eta)z} + a_- \begin{pmatrix} s_2 \\ 1 \end{pmatrix} e^{(\alpha_- + i\eta)z}, \quad (44)$$

where

$$s_{1,2} = se^{\pm i\chi}, \quad s = \kappa / (\Delta + i\bar{\alpha} + \eta)$$

and

$$\eta = \text{sgn}(\Delta) \cdot \{(\Delta + i\bar{\alpha})^2 - \kappa^2\}^{1/2},$$

$$\bar{\alpha} = (\alpha_+ + \alpha_-)/2, \quad \alpha_d = (\alpha_+ - \alpha_-)/2.$$

The above expressions correspond to those used by Denisov and Reznikov [46] and by Bratman et al. [47]. Yet, these authors neglected the exponent Δ in the representation of the total field because it is small compared to the propagation constants β which define the dispersion relation of the modes in a perturbed waveguide. From (3)–(5), (16), (41), and (44), we obtain the propagation constants β_{\pm} for the forward and the backward propagating modes

$$\tilde{\beta}_{\pm} = \beta_{\pm} \pm (\eta - \Delta). \quad (45)$$

$$f_{+p-q} = i \frac{a_1}{2a} \frac{(k_{c+p}k_{c-q}a)^2 + m_+m_-(k^2 - \beta_+ \beta_-)}{\sqrt{[(k_{c+p}a)^2 - m_+^2] [(k_{c-q}a)^2 - m_-^2]} \sqrt{-\beta_+ \beta_-}} \quad \text{TE/TE} \quad (49c)$$

Equation (44) implies that the modes of the perturbed waveguide revert continuously to those of the unperturbed waveguide. This feature is missing in the formalisms of other authors.

For an unperturbed cylindrical metal waveguide of circular cross section and symmetry G_0 , the forward propagating modes $+p = \{m_+, n_+\}$ can be represented by the scalar wave potentials [14]

$$u_{+p}(r, \phi, z) = N_{+p} J_{|m_+|}(k_{c+p}r) e^{im_+\phi} e^{-i\beta_+z}, \quad (46)$$

where (r, ϕ, z) denotes the cylindrical coordinates, N_{+p} the normalization factor of the mode $+p$, $J_m(\rho)$ the Bessel function of the order m , and k_{c+p} the cut-off circular wavenumber given by the n_{+p} -th solution of the equation

$$J_{|m_+|}(k_{c+p}a) = 0 \quad \text{for TM modes} \quad (47a)$$

or

$$\frac{d}{da} J_{|m_+|}(k_{c+p}a) = 0 \quad \text{for TE modes}, \quad (47b)$$

where a represents the radius of the unperturbed cylindrical waveguide of circular cross section.

If we introduce the mode $+p$ defined by the wave potential (46) and a counterpropagating mode $-q$ with an equivalent potential in the overlap integral (25), we find the following general selection rule for mode coupling

$$m_{+p} + m_{-q} - \bar{m} = 0, \quad (48)$$

where m_{+p} and m_{-q} denote the azimuthal mode numbers of the coupling modes of the unperturbed waveguide and \bar{m} characterizes the symmetry of the perturbation according to Table 1 and (30).

This rule can also be derived by group theoretical considerations [14]. An equivalent rule was also applied by Bratman et al. [47]. The different signs which occur in their selection rule originate in a different definition of the wave potentials for the counterpropagating modes. The coupling constants f_{+p-q} can be evaluated directly with the overlap integral (25) and the definitions (21) and (22). For a circular cylindrical waveguide, we find

$$f_{+p-q} = i \frac{a_1}{2a} \frac{k^2 - \beta_+ \beta_-}{\sqrt{-\beta_+ \beta_-}} \quad \text{TM/TM}, \quad (49a)$$

$$f_{+p-q} = \frac{a_1}{2a} \frac{m_{\text{TE}}}{\sqrt{(k_{c,\text{TE}}a)^2 - m_{\text{TE}}^2}} \frac{k(\beta_+ - \beta_-)}{\sqrt{-\beta_+ \beta_-}} \quad \begin{matrix} \text{TE/TM} \\ \text{TM/TE} \end{matrix} \quad (49b)$$

which implies that the phase factor χ introduced in (40) vanishes. From (49b), we conclude that no cross-couplings with TE_{0n} are possible. It should be noticed that (49) agree with those derived by Denisov and Reznikov [46] if the difference in the definition of the wave potential is taken into account. Equations (49) can be transformed into those given by Schill and Seshadri [48]. Their equations contain an additional term which corresponds to the small term neglected in (23b). Equations (49) are also equivalent to those recently presented by Palmer [55] with one exception. In Palmer's TE/TE coupling, the first term in the numerator of (49c) is missing. This would exclude a coupling for m_{+p} and/or m_{-q} equal zero.

1.5. Modified Dispersion Relation of a Two-Mode Coupling

In general, the dispersion relation of an electromagnetic wave in a waveguide expresses the propagation constant of the wave as a function of the free-space

frequency or wavelength. For specific experimental conditions, however, it can be advantageous to choose another variable to represent the variation of the propagation constant. In this study, we are bound to a fixed wavelength of $496.1 \mu\text{m}$ characteristic for the methyl fluoride as active medium in our waveguide lasers. Instead of the wavelength, we have varied in our experiments the period or pitch L defined in Table 1. The corresponding modified dispersion relation is then described by

$$\tilde{\beta}(L) = \text{Re}\{\tilde{\beta}(L)\} + i \text{Im}\{\tilde{\beta}(L)\}, \quad (50)$$

where $\lambda_g = 2\pi/\text{Re}\{\tilde{\beta}(L)\}$ denotes the guide wavelength. This relation can be derived from the dispersion relation (45). For real and imaginary parts of $\tilde{\beta}(L)$, we find for a two-mode coupling

$$\text{Re}\{\tilde{\beta}(L)\} = \beta_+ - \Delta(L) + \text{Re}\{\eta(L)\}, \quad (51a)$$

$$\text{Im}\{\tilde{\beta}(L)\} = \text{Im}\{\eta(L)\}, \quad (51b)$$

where $\Delta(L)$ is given by (42).

A typical modified dispersion relation according to (51) is plotted in Fig. 2 for an ideally conducting waveguide without gain or loss ($\bar{\alpha} = 0$). The geometrical parameters are chosen identically to those of one single-helix HFB waveguide used in our experiments with an oversize factor $f = 2a/\lambda = 9.77$ and the first Fourier coefficient $a_1 = 75.0 \mu\text{m}$ of the perturbation.

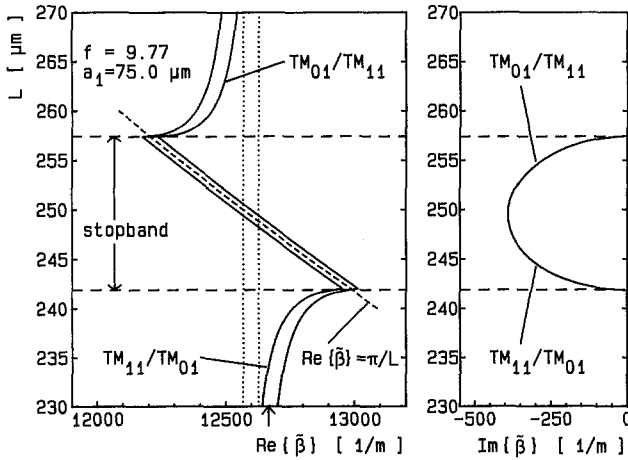


Fig. 2. Modified dispersion relation of a two-mode coupling in a passive ($\bar{\alpha} = 0$) right-handed single-helix HFB waveguide of infinite length with oversize factor $f = 9.77$ and first Fourier coefficient $a_1 = 75.0 \mu\text{m}$. The corrugation pitch L is plotted versus real and imaginary parts of the propagation constant $\tilde{\beta}$. The two solid curves display a forward running TM_{11} mode coupling into a backward running TM_{01} mode and vice versa. Both are symmetrically arranged around the Bragg condition $\text{Re}\{\tilde{\beta}\} = \pi/L$ given by the dashed hyperbola. The two dotted lines represent the TM_{11} mode (left) and the TM_{01} mode (right) of the unperturbed waveguide. The arrow on the abscissa marks $\text{Re}\{\tilde{\beta}\} = k$ where $v_{\text{ph}} = c$.

The two solid curves represent the two possible couplings between a TM_{01} and a TM_{11} mode. Because of the different cut-off wavenumbers for the two modes, they appear symmetrically displaced from the hyperbola given by $\text{Re}\{\tilde{\beta}\} = \beta_0 = \pi/L$ which is indicated by a dashed line. Both couplings are equivalent and cannot be distinguished in their resonances. As a consequence, a resonant HFB or DFB laser mode is always two-fold degenerate. Without gain or loss ($\bar{\alpha} = 0$), η is real outside the stopband ($|\Delta| > |\kappa|$) and imaginary inside the stopband ($|\Delta| < |\kappa|$). The exponential damping of a wave in the stopband is guaranteed by the equation

$$\lim_{\bar{\alpha} \rightarrow 0^-} \text{sgn}(\bar{\alpha}) = -1. \quad (52)$$

If we introduce a weak loss or gain ($\bar{\alpha} \neq 0$), the sharp band edges become rounded, and in the case of gain ($\bar{\alpha} > 0$), the imaginary part $\text{Im}\{\tilde{\beta}\}$ changes sign. The arrow in Fig. 2 on the horizontal axis marks the position where $\text{Re}\{\tilde{\beta}\} = k = 2\pi/\lambda$, i.e. where the phase velocity v_{ph} of the propagating mode falls short of the speed of light c . The two dotted lines indicate the propagation constants of the unperturbed waveguide modes TM_{01} and TM_{11} . The left shows that of the TM_{11} mode and the right that of the TM_{01} mode.

1.6. Resonance Conditions

While the dispersion relation of the modes of axially periodic and helical laser structures are strictly valid for infinite length, the corresponding resonance conditions are determined by the boundary conditions at the ends of the structure. These boundary conditions have to be applied to the solution of the coupled-wave equation (39). In order to simplify the notation, we rewrite (39) in a more convenient matrix form

$$\mathbf{A} = \mathbf{S}e^{\mathbf{N}z} \mathbf{a} \quad (53)$$

with

$$\mathbf{A} = \begin{pmatrix} \mathbf{A}_+ \\ \mathbf{A}_- \end{pmatrix}, \quad \mathbf{S} = \begin{pmatrix} \mathbf{S}_{++} & \mathbf{S}_{+-} \\ \mathbf{S}_{-+} & \mathbf{S}_{--} \end{pmatrix},$$

$$e^{\mathbf{N}z} = \begin{pmatrix} e^{\mathbf{N}_+ z} & 0 \\ 0 & e^{\mathbf{N}_- z} \end{pmatrix}, \quad \mathbf{a} = \begin{pmatrix} \mathbf{a}_+ \\ \mathbf{a}_- \end{pmatrix}.$$

\mathbf{A}_+ and \mathbf{A}_- denote the two vectors corresponding to the m forward and the n backward propagating modes. \mathbf{S} is a matrix with the eigenvectors \mathbf{s}_j taken as columns, and \mathbf{N} a diagonal matrix consisting of the eigenvalues $-i\eta_j$, $j = 1, 2, \dots, (m+n)$ with $\text{Re}\{-i\eta_j\} < 0$ for $j = 1, 2, \dots, m$ and $\text{Re}\{-i\eta_j\} > 0$ for $j = m+1, m+2, \dots, (m+n)$, corresponding to the eigenvectors \mathbf{s}_j . Both \mathbf{S} and \mathbf{N} are divided into submatrices, with \mathbf{S}_{++} and \mathbf{N}_+ being of dimension $(m \times m)$, \mathbf{S}_{--} and \mathbf{N}_- of dimension $(n \times n)$, and \mathbf{S}_{+-} and \mathbf{S}_{-+} of dimensions

$(m \times n)$ and $(n \times m)$ respectively. \mathbf{a}_+ and \mathbf{a}_- are vectors containing m and n arbitrary constants.

We consider a laser structure of length R between $z=0$ and $z=R$ and choose as boundary conditions [3]

$$\mathbf{A}_+(0)=0; \quad \mathbf{A}_-(R)=0. \quad (54)$$

If we apply these boundary conditions to (53), we find

$$\begin{pmatrix} \mathbf{S}_{++} & \mathbf{S}_{+-} \\ \mathbf{S}_{-+} e^{N+R} & \mathbf{S}_{--} e^{N-R} \end{pmatrix} \begin{pmatrix} a_+ \\ a_- \end{pmatrix} = 0. \quad (55)$$

The nontrivial solution of this equation represents the self-consistent oscillation of the laser structure and thus, determines the resonance condition. It only exists if the determinant of the matrix of the system of (55) vanishes. This results in

$$\det(\mathbf{I} - \mathbf{S}_{++}^{-1} \mathbf{S}_{+-} e^{-N-R} \mathbf{S}_{--}^{-1} \mathbf{S}_{-+} e^{N+R}) = 0, \quad (56)$$

where \mathbf{I} indicates the unit matrix. This equation determines the resonances and their corresponding threshold gains.

An alternative method to evaluate the resonances and the threshold gains makes use of the transmission matrix. For this purpose, we introduce the modified boundary conditions

$$\mathbf{A}_+(0) = \mathbf{A}_0; \quad \mathbf{A}_-(R) = 0 \quad (57)$$

in (53) and evaluate the matrix \mathbf{t} of the amplitude transmission defined by

$$\mathbf{A}_+(R) = \mathbf{t} \mathbf{A}_+(0). \quad (58)$$

Thus, we find

$$\mathbf{t} = \mathbf{S}_{++} \{ \mathbf{I} - \mathbf{S}_{++}^{-1} \mathbf{S}_{+-} \mathbf{S}_{--}^{-1} \mathbf{S}_{-+} \} e^{N+R} \times \{ \mathbf{I} - \mathbf{S}_{++}^{-1} \mathbf{S}_{+-} e^{-N-R} \mathbf{S}_{--}^{-1} \mathbf{S}_{-+} e^{N+R} \}^{-1} \mathbf{S}_{++}^{-1}. \quad (59)$$

If we compare this expression with (56), we recognize that the determinant $\det(\mathbf{t})$ of the transmission matrix \mathbf{t} contains the inverse determinant of the resonance condition. For this reason, $\det(\mathbf{t})$ becomes singular at the resonances. The method based on $\det(\mathbf{t})$ is advantageous for the numerical calculations of the resonances and their threshold gains.

A similar method applies the reflection matrix \mathbf{r} defined by

$$\mathbf{A}_-(0) = \mathbf{r} \mathbf{A}_+(0). \quad (60)$$

If we apply the boundary conditions (57) and the above definition (60) to (53), we obtain

$$\mathbf{r} = \{ \mathbf{S}_{-+} - \mathbf{S}_{--} e^{-N-R} \mathbf{S}_{--}^{-1} \mathbf{S}_{-+} e^{N+R} \} \times \{ \mathbf{I} - \mathbf{S}_{++}^{-1} \mathbf{S}_{+-} e^{-N-R} \mathbf{S}_{--}^{-1} \mathbf{S}_{-+} e^{N+R} \}^{-1} \mathbf{S}_{++}^{-1}. \quad (61)$$

$\det(\mathbf{r})$ also contains the inverse determinant of the resonance condition (56) and can, therefore, be applied

in order to determine the resonances of multi-mode couplings.

For two-mode couplings, the expressions corresponding to (59) and (61) were derived by Gnepf and Kneubühl [4]. In the case of two counterpropagating modes, the submatrices in (53) are scalars. If we identify these scalars with the parameters of solution (44) of the two-mode coupling, we find the following resonance condition

$$s^2 e^{-2\eta R} = 1 = e^{-2\pi\tilde{q}}; \quad \tilde{q} = 0, \pm 1, \pm 2, \pm 3, \dots, \quad (62)$$

where \tilde{q} labels the longitudinal DFB or HFB modes. $\tilde{q}=0$ defines a resonance in the center of the stopband [4]. This so-called gap mode cannot oscillate in a waveguide with homogeneous periodic or helical perturbation and symmetric boundary conditions. However, this mode becomes active if the symmetry of the boundary condition is broken [56–59] or by the introduction of a gap in the waveguide [34–36, 60] or by an otherwise produced phase shift [46]. Since we consider neither asymmetric boundary conditions nor built-in phase shifts, the gap mode with $\tilde{q}=0$ is excluded.

In order to evaluate the resonances of DFB and HFB laser systems with gain ($\tilde{\alpha} > 0$), we split (62) into real and imaginary parts. After some transformations, we find

$$\text{Re}\{\eta\} = R^{-1} \cdot \{\pi\tilde{q} + \arg(s)\}, \quad (63a)$$

$$\text{Im}\{\eta\} = -R^{-1} \cdot \ln|s|. \quad (63b)$$

The $\arg(s)$ is positive for negative mode numbers \tilde{q} and vice versa. The position of the resonances are given by the modified resonance propagation constant

$$\tilde{\beta}_{\text{res}} = (\tilde{\beta}_+ - \tilde{\beta}_-)/2 = (\pi/L) + \eta \quad (64)$$

introduced by Wildmann et al. [36] on the basis of the round-trip condition for resonance. With this relation (64), we derive from (63a) the resonance condition

$$\text{Re}\{\tilde{\beta}_{\text{res}}\} = (\pi/L) \cdot [1 + M^{-1} \{\tilde{q} + \pi^{-1} \arg(s)\}] = 2\pi/\lambda_{g,\text{res}}, \quad (65)$$

where $M = R/L$ indicates the number of periods of the laser structure and $\lambda_{g,\text{res}}$ the resonance guide wavelength. In the limit of vanishing threshold gains, i.e. $\tilde{\alpha}^{\text{th}} = 0$ and $\arg(s) = 0$, we obtain the resonances from the intersections between the curves

$$\text{Re}\{\tilde{\beta}_{\text{res}}\} = (\pi/L) + (\pi\tilde{q}/R), \quad (66a)$$

$$\text{Re}\{\tilde{\beta}_{\text{res}}\} = (\pi/L) + \text{Re}\{\eta(L)\}. \quad (66b)$$

In this case, the resonant perturbation periods $L(\tilde{q})$ can be represented by

$$L(\tilde{q}) = (\lambda/2) \cdot [(w_+ + w_-)/2 - \text{sgn}(\tilde{q})(\lambda/2) \{(\tilde{q}/R)^2 + (\kappa/\pi)^2\}]^{-1}, \quad (67)$$

where λ is the free-space wavelength of the laser emission, w_+ and w_- denote the normalized propagation constants of the forward and backward propagating modes of the unperturbed waveguide

$$w_{\pm} = |\beta_{\pm}/k| = \{1 - (ak_{c\pm}/\pi f)^2\}^{1/2}. \quad (68)$$

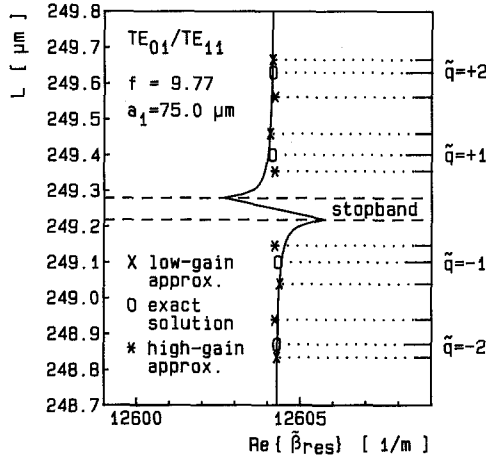


Fig. 3. Comparison between the high-gain and the low-gain approximations as well as the exact solution of the resonance condition for the weak TE_{01}/TE_{11} coupling in a right-handed HFB waveguide with oversize factor $f=9.77$ and first Fourier coefficient $a_1=75.0 \mu\text{m}$. The solid curve shows the corrugation pitch L versus the real part of the resonant propagation constant β_{res} in the low-gain approximation ($\bar{\alpha}^{\text{th}} \approx 0$). The crosses (\times), asterisks ($*$), and the open circles (\circ) denote the resonant pitches L_q for the lowest longitudinal modes \tilde{q} as given by the low-gain and the high-gain approximations as well as those from the exact solution of the resonance condition for two-mode coupling

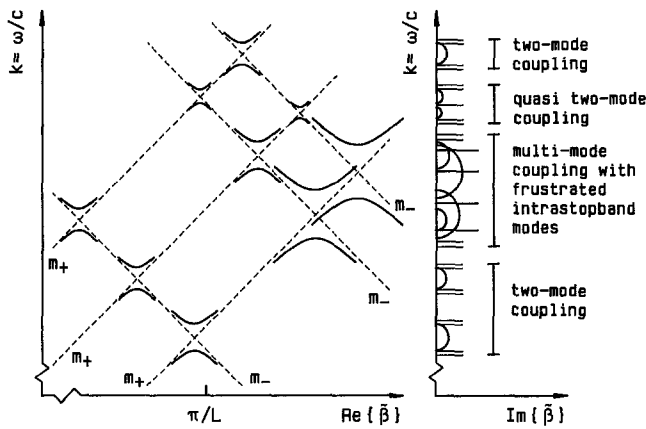


Fig. 4. Schematic representation of a multi-mode coupling between three forward (m_+) and three backward (m_-) propagating modes. All nine possible two-mode couplings are assumed as allowed, yet of different strengths. The resulting resonance frequency spectrum, illustrated in the plot of the imaginary part of the propagation constant β , can be divided into three categories depending on the degree of interaction between the various two-mode couplings

Far from cut-off, w_{\pm} fulfil the condition

$$(w_+ + w_-)/2 \approx 1 \quad (69)$$

which implies $L(\tilde{q}) \approx \lambda/2$.

For mode couplings where the threshold gains of the longitudinal modes are not neglectable compared to the coupling strength, the term $\arg(s)$ of (65) causes a shift of the hyperbolas given by (66a) towards the stopband edges.

In Fig. 3, the resonances of the four lowest longitudinal modes next to the stopband of the TE_{01}/TE_{11} coupling in a single-helix HFB waveguide are plotted under three different conditions. The geometrical waveguide parameters, $f=2a/\lambda=9.77$ and $a_1=75.0 \mu\text{m}$, are chosen typical to those of the waveguides used in this work. The solid curve represents the limit of low-gain approximation ($\bar{\alpha}^{\text{th}} \ll |\kappa|$). The crosses mark the resonances for different values of \tilde{q} . On the right vertical axis the corresponding resonant pitches of perturbation are depicted as horizontal bars. Since the coupling coefficient of the considered coupling is small compared to the threshold gains ($\bar{\alpha}^{\text{th}} > 8 \text{ m}^{-1}$) given by (62), the rounding of the stopband edges is significant. As a consequence, the resonant pitches represented by circles which correspond to the exact solution of the resonance condition deviate significantly from the low-gain approximation. For comparison, also the solutions of the high-gain approximation limit ($\bar{\alpha}^{\text{th}} \gg |\kappa|$) characterized by $\arg(s) = \pi/2$ are shown as asterisks in the plot.

In our waveguides, essentially all possible couplings are considerably stronger than that shown in Fig. 3. Since, moreover, the threshold gains vary approximately inversely proportional to the square of the coupling strength, the low-gain approximation, i.e. (67) gives a good estimation for two-mode resonances observed in our experiments.

The theoretical investigations on the mode spectra of multi-mode couplings have mostly been performed by numerical calculations making use of the transmission matrix (59) because it was found that the roots of (56) are more difficult to evaluate than the equivalent poles of (59). As in the case of a two-mode coupling, all modes present in a multi-mode coupling obey the selection rule (48). For a specific multi-mode coupling defined by the pair (m_+, m_-) according to the selection rule (48), we have to presume that the resonance frequencies of waveguide modes with the azimuthal mode number m_+ or m_- lie very close. These modes are separated in two sets defined by m_+ and m_- . A mode within one set couples only with a mode in the other set in accordance with the actual waveguide symmetry.

When considering the frequency spectrum of multi-mode couplings, one has to distinguish the three cases illustrated in Fig. 4. For the simple case A the multi-

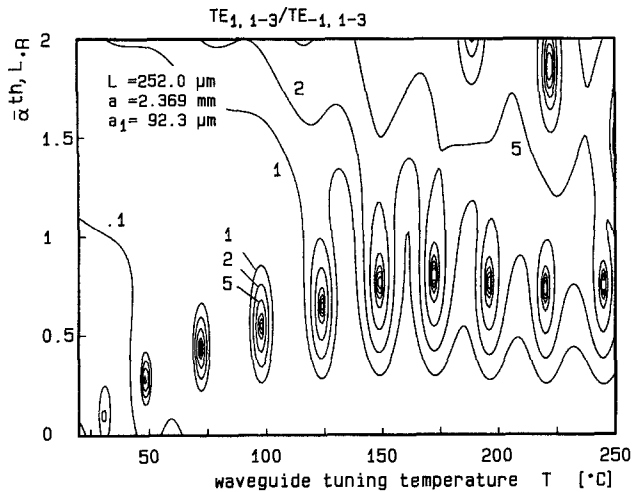


Fig. 5. Contour lines corresponding to fixed values of the transmission determinant $\det(\mathbf{t})$ in the plane defined by the waveguide tuning temperature T and the normalized effective threshold gains $(\bar{\alpha}^{\text{th},L} \cdot R)$ of a multi-mode coupling between the TE_{1n} forward propagating and the TE_{-1n} backward propagating sets of modes in a periodic DFB copper waveguide with corrugation period $L=252.0 \mu\text{m}$, mean radius $a=2.369 \text{ mm}$, and first Fourier coefficient $a_1=92.3 \mu\text{m}$. In this given temperature range between 22°C and 250°C , the resonances observed are characteristic for modes of a quasi two-mode coupling

mode coupling consists of widely separated two-mode couplings without mutual interaction. Thus, the resulting multi-mode spectrum is the sum of the spectra of the individual two-mode couplings. On the other hand, when modes with partially or totally overlapping two-mode stopbands are combined, a large multi-mode stopband arises. In this case C, resonances similar to those of the two-mode case A exist outside the two edges of the wide multi-mode stopband. In addition, also intrastopband resonances emerge. In contrast to the ingap modes generated by a phase shift, e.g. by a gap in the periodic waveguide structure [34–36, 60], these new frustrated intrastopband modes usually show considerably higher threshold gains than the resonances outside the stopband edges. An intermediate case B occurs when the multi-mode coupling consists of relatively weak two-mode couplings which do not overlap, yet have noticeable mutual interaction. Under this condition, one observes a repulsion of the neighbouring stopband edges together with a frequency shift of the resonances. The threshold gains of these shifted quasi two-mode resonances are usually higher yet of the same order of magnitude as those of the standard resonances of the related two-mode couplings.

The two contour plots of Figs. 5 and 6 represent cases B and C of multi-mode couplings. The abscissa

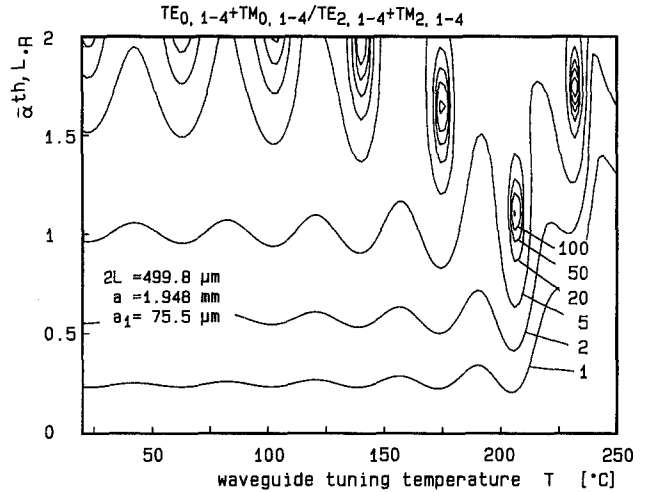


Fig. 6. Contour lines corresponding to fixed values of the transmission determinant $\det(\mathbf{t})$ in the plane defined by the waveguide tuning temperature T and the normalized effective threshold gains $(\bar{\alpha}^{\text{th},L} \cdot R)$ of a multi-mode coupling between the TE_{0n} and TM_{0n} forward running and the TE_{2n} and TM_{2n} backward propagating sets of modes in a double-helix HFB brass waveguide with corrugation pitch $2L=499.8 \mu\text{m}$, mean radius $a=1.948 \text{ mm}$, and first Fourier coefficient $a_1=75.5 \mu\text{m}$. In this given temperature range between 22°C and 250°C , the resonances observed are characteristic for the so-called frustrated intrastopband modes

corresponds to the waveguide temperature T of a periodic DFB copper waveguide of period $L=252.0 \mu\text{m}$ for Fig. 5 and of a double-helix HFB brass waveguide of pitch $2L=499.8 \mu\text{m}$ for Fig. 6. In this context, it should be mentioned that these waveguides are tuned by thermal expansions at the fixed wavelength $\lambda=496.1 \mu\text{m}$ of the methyl fluoride laser emission, cf. Sect. 2.2. The ordinate indicates the normalized threshold gain $\bar{\alpha}^{\text{th},L} \cdot R$ for a lossy waveguide, where R denotes the total length of the waveguide structure. The contour lines correspond to fixed values of the determinant $\det(\mathbf{t})$ of the transmission matrix \mathbf{t} introduced by (59). At a two-mode or multi-mode resonance, $\det(\mathbf{t})$ approaches infinity. In Figs. 5 and 6, the waveguide parameters and the temperature range correspond to our experimental conditions, cf. Sect. 2. The resonances observed in Fig. 5 corresponding to case B represent a multi-mode coupling between the $m_+ = +1$ and $m_- = -1$ sets, each consisting of three TE modes of the DFB waveguide. The series of the observed resonances with low threshold gains are quasi two-mode resonances shifted from the mutual interaction region of the pure $\text{TE}_{11}/\text{TE}_{-11}$ and the $\text{TE}_{11}/\text{TE}_{-13}$ two-mode couplings. In the case C, illustrated in Fig. 6, we deal with a multi-mode coupling between the $m_+ = 0$ and $m_- = +2$ sets of modes each consisting of four TE and four TM modes of a

double-helix HFB waveguide. In this case, there exist many overlapping two-mode couplings of similar strength. As a result, we observe frustrated intrastop-band modes inside the wide multi-mode stopband. The mode at the waveguide temperature $T=205^\circ\text{C}$ exhibits a low threshold gain compared to all other calculated resonances in this temperature range and could therefore result in HFB laser oscillation.

From a comparison between the threshold gains of the resonances of both two-mode and multi-mode couplings, we conclude that the resonances originating in simple two-mode couplings are more likely to oscillate than those generated by complex multi-mode couplings.

1.7. Waveguide Loss in the FIR

In Sect. 1.4, we introduced the effective gains α_{+p} and α_{-q} for the forward and backward propagating modes. Since the waveguide is, however, not ideal, these effective gains represent the differences between proper gains and the corresponding waveguide losses. Consequently, we write

$$\alpha_{+p} = \alpha_{+p}^G - |\alpha_{+p}^L|; \quad p = 1, 2, \dots, m, \quad (70a)$$

$$\alpha_{-q} = \alpha_{-q}^G - |\alpha_{-q}^L|; \quad q = 1, 2, \dots, n. \quad (70b)$$

In order to evaluate the true threshold gain for a resonance labelled \tilde{q} in a lossy waveguide, we have to correct the corresponding gain of (56) by a resonance-independent function which includes the loss terms of all participating modes

$$\tilde{\alpha}_{\tilde{q}}^{\text{th},L} = \tilde{\alpha}_{\tilde{q}}^{\text{th},0} + B(|\alpha_{+p}^L|, |\alpha_{-q}^L|). \quad (71)$$

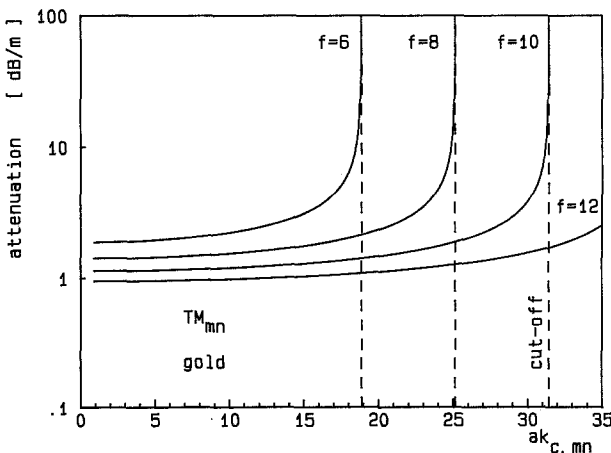


Fig. 7. Field attenuation for TM modes in a gold covered waveguide versus the generalized continuous root $ak_{c,mn}$ of the corresponding Bessel function for four different oversize factors f . The dashed vertical lines denote the respective cut-off values $ak_{c,mn} = \pi f$

Since the medium gain must compensate the losses, we have to require a positive function B . For multi-mode couplings it is not possible to represent B in a closed form. Therefore, the only way to determine the medium threshold gain is to solve (56) with the complete expression for the effective gain described by (70). For a two-mode coupling, however, we can derive from (44) and (62) the following simple expression for the loss function

$$B(|\alpha_{+p}^L|, |\alpha_{-q}^L|) = (|\alpha_{+p}^L| + |\alpha_{-q}^L|)/2 = |\bar{\alpha}^L|. \quad (72)$$

Thus, the medium threshold gain is simply evaluated by adding the mean value of the mode losses to the effective threshold gain given by (62).

The waveguide loss in the far infrared is well defined by the standard skin effect. For hollow metal waveguides, this loss was described by Borgnis and Papas [49]. For a circular symmetry, we find for the two possible types of modes

$$\alpha_{mn} = -(2/fw_{mn}) \cdot (\pi/\sigma c \mu_0 \lambda^3)^{1/2} \quad \text{TM modes}, \quad (73a)$$

$$\alpha_{mn} = -(2/fw_{mn}) \cdot (\pi/\sigma c \mu_0 \lambda^3)^{1/2} \times \frac{(ak_{c,mn}/\pi f)^2 + (mw_{mn}/ak_{c,mn})^2}{1 - (mw_{mn}/ak_{c,mn})^2} \quad \text{TE modes}, \quad (73b)$$

where m and n denote the azimuthal and radial mode numbers of the propagating mode. $k_{c,mn}$ is the corresponding cut-off wavenumber defined by (47) and a the waveguide radius. σ indicates the dc conductivity whilst c and μ_0 are the speed of light and the permeability of vacuum. In the above equations (73), we also use the oversize factor $f=2a/\lambda$ and the normalized propagation constant w_{mn} defined by (68).

Although the $ak_{c,mn}$ are discrete, we have plotted for simplicity the attenuation $|\alpha_{mn}|$ versus the corresponding continuous parameter $ak_{c,mn}$ for a gold waveguide. The wavelength $\lambda=496\ \mu\text{m}$ corresponds to the dominant emission of the CH_3F laser. In Fig. 7, we show the attenuation of the TM modes for four different oversize factors f . Characteristic for TM modes are the monotonous growth of the waveguide loss with increasing $ak_{c,mn}$ and the phenomenon that all modes experience approximately the same attenuation as long as they are sufficiently distant from the cut-off given by $ak_c = \pi f$. On the other hand, the attenuation of the TE modes behaves more complicated as demonstrated in Fig. 8. Firstly, the dependence of the attenuation on the magnitude on the azimuthal mode number $|m|$ is evident for small $ak_{c,mn}$ and secondly, all curves except those for $m=0$ are characterized by a local minimum. The latter implies that only for $m=0$ the mode with lowest attenuation coincides with that of lowest $ak_{c,mn}$.

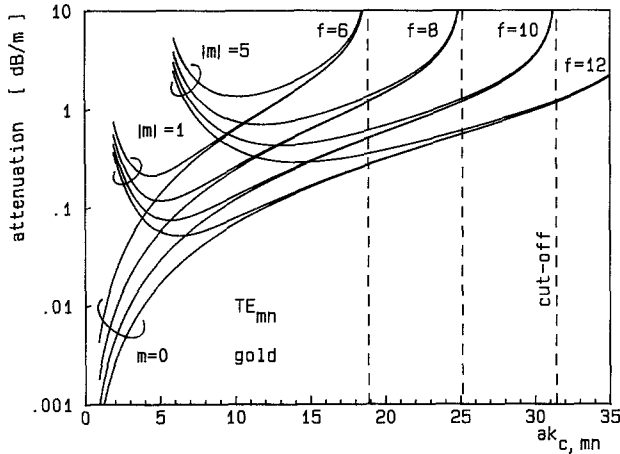


Fig. 8. Field attenuation for TE modes in a gold covered waveguide versus the generalized continuous root $ak_{c,mn}$ of the derivative of the corresponding Bessel function for four different oversize factors f . The different sets of curves are characterized by the magnitude of the azimuthal mode number $|m|$. The dashed vertical lines denote the respective cut-off values $ak_{c,mn} = \pi f$

1.8. Gain Saturation

From the resonance condition (62), we find for a strong two-mode coupling ($\bar{\alpha}_q^{\text{th}} \ll |\kappa|$), which is also called overcoupling, an approximate expression for the threshold gain for DFB and HFB resonances in the vicinity of the stopband edges by neglecting the waveguide loss [34–36]

$$\bar{\alpha}_q^{\text{th},0} \cdot R \simeq (\pi \bar{q} / |\kappa| R)^2. \quad (74)$$

This expression implies a quadratic increase of the threshold gain with growing longitudinal mode number. This relation implies that the strongest laser output should occur for the lowest magnitude $|\bar{q}|$ of the mode number \bar{q} . Since, however, the gain of the laser medium cannot be assumed to remain constant for growing field intensity, nonlinear gain saturation has to be taken into account when describing the output characteristics of strongly coupled resonances with strong intracavity fields. Hill and Watanabe [62] first postulated a model including the envelope-gain saturation. In this context, they calculated the influence of gain saturation on the resonance frequencies as well as the small-signal gain required for a given output power for various coupling strengths. In the same year, Haus [63] devised an approximate method for the calculation of the small-signal gain as a function of the normalized output power for overcoupled ($|\kappa|R > 4$) DFB resonances. This method was later improved by Szczepanski [64] to allow for lower coupling strengths ($|\kappa|R > 0.1$). Furthermore, extended models have been presented which include reflections at the ends of the DFB structure [65–67]. All these efforts, however, have been devoted to the optimization of laser design,

yet not to the interpretation of the behaviour of an operating DFB or HFB laser.

Since all couplings in the laser waveguides we have investigated yield coupling strengths considerably larger than $|\kappa|R = 1$, we observe in accordance with the predictions by Hill and Watanabe [62] no shift in the resonance frequencies caused by gain saturation. Therefore, we can calculate the location of our resonances by assuming linear coupling according to (43) and (62). If we assume, in contrast to the previously mentioned papers, that the small-signal gain of a given coupling is known, we can apply a modification of the approach by Haus [63] to calculate the relative output power for all consecutive longitudinal modes. A subsequent comparison with the measured spectra provides us the best fit of the experimentally determined small-signal gain. The results obtained by this procedure show a qualitatively good agreement with our observed resonances and their relative output power (Sect. 2). Therefore, a brief description of the method is worthwhile.

An energy-conservation theorem for a two-mode coupling can be derived from the coupled-wave equation (43). In our notation, this theorem can be formulated as follows

$$\begin{aligned} |A_+(R)|^2 + |A_-(0)|^2 \\ = 2 \int_0^R (\bar{\alpha}^G - |\bar{\alpha}^L|) (|A_+|^2 + |A_-|^2) dz. \end{aligned} \quad (75)$$

Here, we make use of the fact that the effective gain and loss in the waveguide during one cycle correspond to the average of the two individual gains and losses given by (71) and (72). In order to include gain saturation, we write the medium gain in the form

$$\bar{\alpha}^G = \alpha_0 / \{1 + (|A_+|^2 + |A_-|^2) / P_s\}, \quad (76)$$

where α_0 and P_s denote the small-signal gain and the saturation power.

According to Kogelnik and Shank [3], the energy per cycle emitted at the waveguide ends is for strong couplings small compared to the energy stored in the structure. Under this assumption, Haus [63] estimated the distributions of A_+ and A_- at resonance for $\bar{\alpha}^G = \bar{\alpha}^L = 0$ near the stopband edges ($|A| \simeq |\kappa|$). Our corresponding result is

$$|A_+| \simeq |A \sin(\eta_0 z)| \simeq |A_-|, \quad (77)$$

where $\eta_0 R = \text{Re}\{\eta R\} = \pi \bar{q}$. With this approximation, the output power at one waveguide end can be evaluated from (43) for the lossless waveguide. Since the output power for a symmetric waveguide corrugation is equal at both ends [62], (43) and (74) imply

$$P \simeq |A_+(R)|^2 = |A_-(0)|^2 \simeq \bar{\alpha}_q^{\text{th},0} R |A|^2. \quad (78)$$

By application of (76)–(78) to the energy theorem (75), we find, after performing the integration over the waveguide length and rearranging the terms, the output power P of the longitudinal mode with number \tilde{q} normalized with respect to the saturation power P_s , to obey the following relation

$$\frac{P}{P_s} = \frac{\bar{\alpha}_{\tilde{q}}^{\text{th},0} R}{8} \left(\left\{ 1 + \frac{8\alpha_0}{\bar{\alpha}_{\tilde{q}}^{\text{th},L}} \right\}^{1/2} - 3 \right) \times \left(\left\{ 1 + \frac{8\alpha_0}{\bar{\alpha}_{\tilde{q}}^{\text{th},L}} \right\}^{1/2} + 1 \right), \quad (79)$$

where $\bar{\alpha}_{\tilde{q}}^{\text{th},0}$ and $\bar{\alpha}_{\tilde{q}}^{\text{th},L}$ are given by (62), (71), and (72). The first factor is monotonically growing with $|\tilde{q}|$ whilst the second is maximum for $|\tilde{q}|=1$ and vanishing for $\bar{\alpha}_{\tilde{q}}^{\text{th},L}=\alpha_0$. Consequently, there exist two resonances $\tilde{q}=\pm|\tilde{q}_{\text{opt}}|$ with maximum output power which, in practice, do not coincide with the longitudinal modes $\tilde{q}=\pm 1$ at the stopband edges.

The influence of the gain saturation of the laser medium on the output power is illustrated in Fig. 9 for a coupling with $|\kappa|R=143$, which is well within the validity range $|\kappa|R>4$ of our approximation. As a consequence of the gain saturation, we find that the output power decreases toward the stopband edges. This in contrast to the predictions of the linear coupled-wave theory.

The behaviour of the relative output power can also be plausibly explained from another point of view. As $|\tilde{q}|$ approaches 1, the magnitude of the scattering factor s for the two-mode coupling given by (44) tends to unity and, consequently, the conversion between the two present modes becomes perfect. Thus, the structure reflection of the waveguide reaches almost 100%

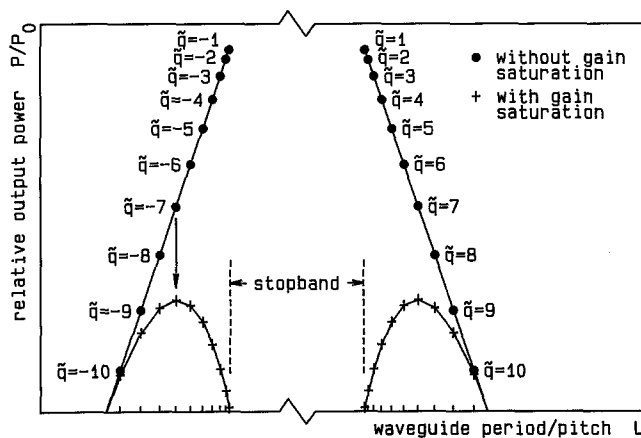


Fig. 9. Comparison of the relative output power of the lowest longitudinal modes \tilde{q} around the stopband of a symmetric DFB or HFB waveguide for a coupling with $|\kappa|R=143$ and a small-signal gain $\alpha_0=0.46\text{ m}^{-1}$. The dots (●) represent a laser medium with gain independent of the field strength whilst the plus sign (+) show the situation when gain saturation is included

which implies that no radiation can emerge from the waveguide ends. This explanation is in agreement with the output characteristics of mirror resonators described in terms of the output-coupler reflectivity.

Equation (79) does not include the effects of spatial hole burning, dispersion of the laser medium, inhomogeneous pumping etc. Therefore, it cannot be expected to explain the full dynamics of a DFB or HFB gas laser. Nevertheless, it is in good qualitative agreement with our experiments on various DFB and HFB couplings in the optically pumped $496\text{ }\mu\text{m}$ CH_3F laser described in the following Sect. 2.

2. Measurements on Waveguide Lasers with Periodic and Helical Corrugations

The first part of this section is devoted to the design and to the operational characteristics of our optically pumped $496\text{ }\mu\text{m}$ CH_3F DFB and HFB gas lasers while the second part comprehends measurements and results. In Sect. 2.1, we present the mechanical data and discuss the manufacture of the different DFB and HFB waveguide structures. In the following Sect. 2.2, we describe the tuning of these waveguide structures by thermal expansion. In Sect. 2.3 and Sect. 2.4, we explain experimental arrangement and the experimental conditions under which our mode spectra were recorded. We elucidate the measured mode spectra of the DFB waveguide lasers as well as of the single- and double-helix HFB waveguide lasers in Sects. 2.5–2.7. Subsequently, we perform a tentative identification of the observed resonant modes on the basis of the perturbation theory outlined in Sect. 1. In addition, we introduce the gain saturation of the laser medium described in Sect. 1.8 to explain the observed output characteristics of the different detected longitudinal DFB and HFB laser modes.

From the numerical evaluations of the resonance conditions for both the two-mode coupling determined by (62) and the complex multi-mode coupling defined by (56), we find, as already mentioned in Sect. 1.6, that for our waveguide and corrugation parameters only the weakest two-mode couplings show threshold gains equivalent to those of the multi-mode couplings. Therefore, we assume that the two-mode couplings dominate over the multi-mode couplings when we attempt to identify the measured resonant DFB and HFB laser emissions. Hence, we first tried to assign the observed resonant modes to potential resonances of two-mode couplings determined by the selection rule (48) and the resonance condition (62). In the last Sect. 2.8 of this chapter, we finally present the output characteristics of various DFB and HFB laser modes as a function of the

polarization state of the pump beam from the CO₂ laser.

2.1. Laser-Waveguide Design and Manufacture

In this study, we have investigated the mode spectra of the 496 μm CH₃F laser equipped with a large variety of hollow circular cylindrical metal waveguides of 300 mm length with periodic or helical corrugations on their inner walls. Three different symmetries of corrugation were chosen. These symmetries correspond to the actually periodic DFB waveguide structure, the single-helix HFB, and the double-helix HFB waveguide structure. With the notations introduced by Preiswerk et al. [14] and discussed in Sect. 1.4, our waveguides can be assigned to the symmetries G_{ps} , G_{hs} , and G_{2hs} respectively.

From group theoretical considerations [14], one finds relations between first order double-helix HFB, second order single-helix HFB, and second order DFB

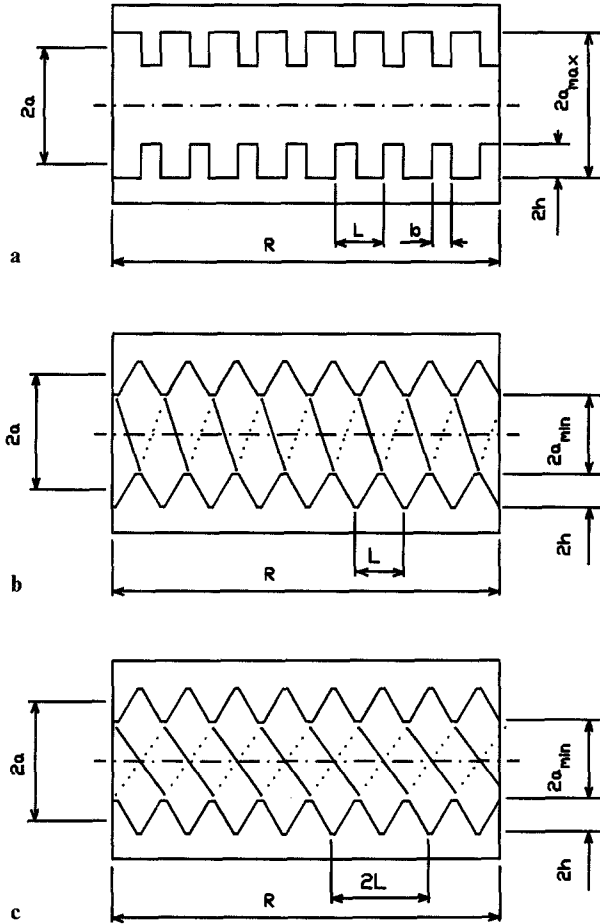


Fig. 10. Schematic view of the circular symmetric FIR-laser waveguides for a) periodic DFB; b) single-helix HFB; c) double-helix HFB. The parameters are defined in the text

which concern periods and pitches of periodic and helical corrugations. Since we restricted our experiments to the laser medium methyl fluoride CH₃F which has its dominant emission at the vacuum wavelength $\lambda = 496.1 \mu\text{m}$, we had to choose the pitch of the double-helix structure about twice the pitch of the single-helix. The latter has to be similar to the period of the linear periodic waveguides to achieve operation of identical order feedback ν (cf. Table 1). In other words, the effective structure period $L \approx \nu\lambda/2$, i.e. the shortest translation along the waveguide axis necessary to reproduce the corrugation has to coincide more or less for all waveguides.

In Fig. 10, we show the geometries of the three investigated types of waveguides. All waveguides are designed for operation at feedback of the first order $\nu = 1$. Consequently and in agreement with the considerations outlined above, we have chosen the effective corrugation period near $L = 250 \mu\text{m}$ for all waveguides. The precise geometrical data of the various investigated types of waveguides together with the respective waveguide materials are presented in Table 2. The first Fourier coefficient a_1 and the mean diameter $2a$ of each corrugation have been evaluated from the known corrugation shape and the depth $2h$ determined by the tool used for cutting. For our DFB and HFB waveguides, the relevant formulae are given in the form

$$2a = 2a_{\max} - (2hb/L) \quad \text{DFB} \quad (80a)$$

$$a_1 = (4h/\pi) \cdot \sin(\pi b/L)$$

and

$$2a \approx 2a_{\min} + 2h \quad \text{HFB.} \quad (80b)$$

$$a_1 \approx (2L\sqrt{3}/\pi^2) \cdot \sin^2(2\pi h/L\sqrt{3})$$

Table 2. Parameters of the investigated waveguides

	DFB	Single-helix HFB	Double-helix HFB
Material	Copper	Brass (58)	Brass (58)
R [mm]	300 ± 1	300 ± 1	300 ± 1
L [μm]	240.0 ± 0.1 244.0 ± 0.1 248.0 ± 0.1 252.0 ± 0.1	250.0 ± 0.1	250.1 ± 0.1
$2a$ [mm]	4.750 ± 0.015	2.850 ± 0.010 3.890 ± 0.010 4.870 ± 0.010 5.890 ± 0.010	3.890 ± 0.010 4.890 ± 0.010
a_1 [μm]	70–95	75–85	70–80

Due to the circular symmetry and the relatively small diameters, the linear periodic waveguide structures cannot be manufactured in one single step. Thus, we first cut periodical grooves into a precision-grinded brass pipe of outer diameter $2a_{\max} = 4.880$ mm. For this purpose, we applied a turning tool of width $b = 124$ μm . The cutting depth and the period were varied from waveguide to waveguide (cf. Table 2). In a second step, the structure was covered with a gold layer by means of vapour deposition. This step was followed by an electrolytic copper deposition onto the gold. The brass pipe was finally etched away to form the definite periodic waveguide structure. The gold layer, which is required for the manufacturing process, also serves as protection of the final periodic waveguide structure against oxidation. Since gold and copper exhibit different thermal expansion coefficients, we have chosen a gold layer of a relatively large thickness of about 50 μm in order to avoid destruction due to thermal stress during the tuning process described in the following Sect. 2.2. The thickness of the gold layer well surpasses the skin depth at our operation wavelength.

In contrast to our DFB waveguides, the single-helix and the double-helix HFB waveguides could be fabricated in one operation. In both cases, we used prebored pipes of 300 mm length made of a brass alloy consisting of 58% copper, 39% zinc, and 3% lead. The helical structures were then cut into the inner waveguide wall with the aid of precision-grinded screw taps with a single-helix or a double-helix corrugation symmetry.

The accuracy of the nominal period L and the nominal pitches L and $2L$ of our different waveguide symmetries taken as an average error over the entire waveguide length R , is by different methods estimated to the order of $\Delta L/L = 4 \times 10^{-4}$. The local accuracy of the linear period, however, may be one order of magnitude worse, since in this case one has to consider the positioning error of the lathe. If, as expected, this variation is randomized around the nominal value, it does not give rise to any consecutively changing phase factor, so-called chirp, in the expression for the corrugation (30), which would result in a shift in the resonance spectrum [61]. In a first approximation, we therefore neglect such local variations. A more critical parameter, however, is the corrugation depth, which by its linear dependence on a_1 can cause a considerable shift of the resonant modes. By manufacturing the periodic waveguides at the tolerance limit and from the indirect measurement of the depth of the helical waveguides mentioned above, we can postulate a relative error of a_1 to $\Delta a_1/a_1 = \pm 10\%$. Since the coupling coefficient κ for all types of coupling is according to (49) proportional to a_1 , we find the same relative error for κ . This

results in an adequate shift of the resonant structure periods or pitches versus the calculated resonance lengths (67). In order to estimate this mismatch of $L_{\tilde{q}}$, we notice the weak a_1 -dependence on $\arg(s)$ near the stopband edges according to (44). Hence, our estimation can be based on the approximation for $L_{\tilde{q}}$ described by (67). We define

$$\Delta L_{\tilde{q}} = L_{\tilde{q}}(a_{1,\text{real}}) - L_{\tilde{q}}(a_{1,\text{est}}) \quad (82)$$

with $a_{1,\text{real}}$ and $a_{1,\text{est}}$ denoting the true and the estimated first Fourier coefficient a_1 of the waveguide structure. In Fig. 11a, we show the shift $\Delta L_{\tilde{q}}$ of the first resonant mode next to the lower stopband edge for various mode couplings in a single-helix HFB waveguide with oversize factor $f=10$ and an estimated

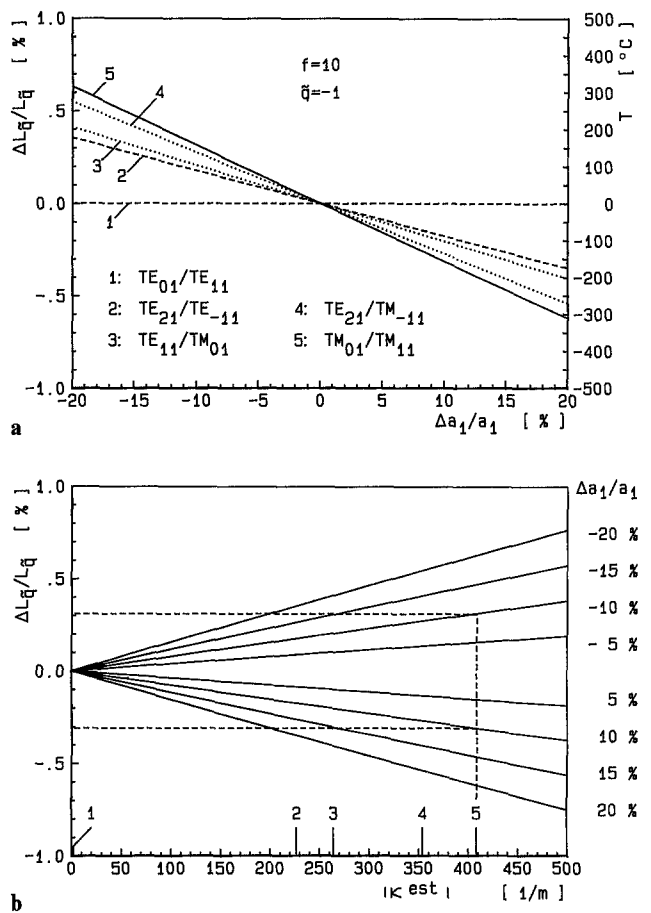


Fig. 11. a Relative shift in the effective resonance period $L_{\tilde{q}}$ (left axis) and resonance temperature (right axis) for a longitudinal mode with $\tilde{q} = -1$ in a waveguide with oversize factor $f = 10$ versus the relative uncertainty in the corrugation amplitude a_1 plotted for five different two-mode couplings of a single-helix HFB laser waveguide. **b** Relative shift in the effective resonance period $L_{\tilde{q}}$ versus the estimated coupling strength κ^{est} for various relative uncertainties in the corrugation amplitude a_1 in a waveguide with oversize factor $f = 10$. The labelled ticks on the horizontal axis refer to the couplings shown in **a**

Fourier coefficient $a_1 = 80 \mu\text{m}$. On the left vertical axis, we have plotted the relative change in the resonant pitch $\Delta L_{\tilde{q}}/L_{\tilde{q}}$ due to incorrect estimation of the Fourier coefficient, whilst on the right vertical axis, we indicate the corresponding shift in the resonance temperature T for the brass waveguides applied for the HFB lasers (cf. Sect. 2.2) with an average thermal expansion coefficient $\Theta = 2 \times 10^{-5} \text{K}^{-1}$. Whilst the pure TE/TE as well as the cross-couplings show a strong variation between different mode couplings as a result of the complex mode dependence in their coupling coefficients (49), the pure TM/TM couplings remain approximately constant. The pure TE/TE couplings with one $m=0$ are weak and, therefore, insensitive to variations of a_1 , as indicated for the $\text{TE}_{01}/\text{TE}_{11}$ coupling. Characteristic for the descent of the curves is the coupling strength of the considered mode coupling. A plausible proof for this statement which is independent of the mode and holds for all types of couplings and waveguide symmetries can be derived from (67) under the assumption that the oversize factor $f = 2a/\lambda$ is large enough to permit the approximation $|\beta_{\pm}| = k$. If we make use of $|\kappa| \ll k$ which is true for weak waveguide modulations and put $\tilde{q} = 0^-$, we find

$$\frac{\Delta L_{\tilde{q}}}{L_{\tilde{q}}} \simeq - \frac{|\kappa_{\text{est}}|}{k} \frac{\Delta |\kappa|}{|\kappa_{\text{est}}|} = - \frac{|\kappa_{\text{est}}|}{k} \frac{\Delta a_1}{a_1}. \quad (83)$$

The almost linear dependence of $\Delta L_{\tilde{q}}/L_{\tilde{q}}$ on $\Delta a_1/a_1$ which results from a more accurate numerical calculation is presented in Fig. 11b for various errors of estimations concerning the Fourier coefficient. The longer ticks on the horizontal axis mark the actual strengths of the couplings presented in the previous Fig. 11a. If we consider the $\text{TM}_{01}/\text{TM}_{11}$ coupling as an example, a relative error of $\Delta a_1/a_1 = \pm 10\%$ causes a relative shift in the resonance pitch of about $\Delta L_{\tilde{q}}/L_{\tilde{q}} \cong 0.3\%$. This uncertainty which originates in depth and shape of the corrugation is equivalent to $\Delta L \cong \pm 0.75 \mu\text{m}$ or $\Delta T \cong \pm 150^\circ\text{C}$ (cf. Sect. 2.2) for a brass waveguide with the nominal pitch $L = 250 \mu\text{m}$.

2.2. Tuning Mechanism

The homogeneously broadened [68] FIR laser emission at $496.1 \mu\text{m}$ of the optically pumped CH_3F laser has a gain bandwidth of about 120 MHz at our operation pressure of about 3 Torr. Our periodic and helical waveguides of length R have an equivalent free spectral range $c/2R$ of about 500 MHz. Therefore, we require a special tuning mechanism to match the laser emission with the waveguide resonances. For this purpose, we apply the method used by Preiswerk et al. [12–14] which relies on the thermal expansion of the waveguide material. This method involves an indirect heating, where the

waveguide is totally surrounded by a heating jacket which consists of a cylindrical quartz dewar (cf. Sect. 2.3) filled with silicon oil in direct contact with a heating coil. By this method, we attain an almost homogeneous temperature distribution in the waveguide over the entire tuning range from room temperature to about $T = 250^\circ\text{C}$. Our measurements of the thermal distribution have revealed a moderate temperature variation between the center and the ends of the waveguide of a few degrees in the upper temperature range. This deviation corresponds to a frequency shift less than about half the laser bandwidth over the entire tuning range. It can, therefore, be expected that this causes a broadening of the observed resonances and contributes to the variation of the output power among different measurements. It may also increase the mode competition between neighbouring resonant modes because it reduces the precision of the corrugation period or pitch. These resonant modes can be assigned to the corresponding structure period or pitch, when the thermal expansion of the waveguide material is known. Since we are measuring over a relatively wide temperature range, we have to take into account the variation of the thermal expansion with temperature T which is described in a first approximation by the relation

$$x(T)/x_0 = 1 + \Theta_1(T - T_0) + \Theta_2(T - T_0)^2. \quad (84)$$

Here, x represents any of the linear parameters R , L , a , or h or the waveguide. x_0 is the corresponding value at room temperature T_0 . Θ_1 and Θ_2 denote the linear and the quadratic thermal expansion coefficients. In Table 3, we have summarized the approximate coefficients for brass [58], copper, and gold [69, 70] for $T_0 = 20^\circ\text{C}$. With these numbers, we calculate a spectral tuning range for our waveguides made of brass or copper/gold (cf. Sect. 2.1) of approximately 3λ or 2.5λ corresponding to about 3 GHz or 2.5 GHz expressed in terms of frequency. The second values valid for the copper/gold DFB waveguides are evaluated under the assumption that the copper alone is responsible for the expansion. This can be considered as a good approximation since the thickness of the copper is about 50 times that of the $50 \mu\text{m}$ gold layer.

Table 3. Linear and quadratic thermal expansion coefficients of the waveguide materials applied

Material	Θ_1 [K^{-1}]	Θ_2 [K^{-2}]
Brass (58)	18.6×10^{-6}	15.0×10^{-9}
Copper	16.7×10^{-6}	7.2×10^{-9}
Gold	14.2×10^{-6}	5.2×10^{-9}

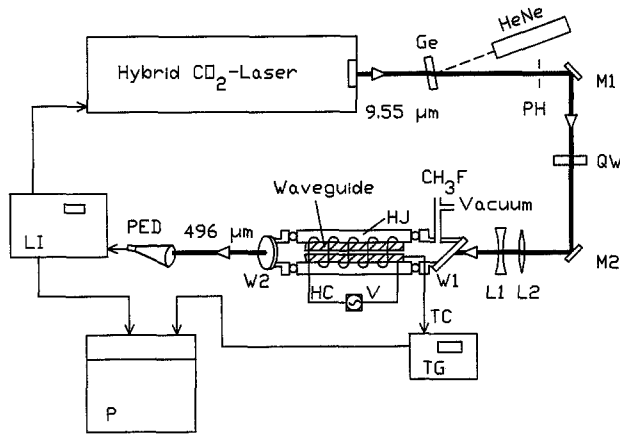


Fig. 12. Experimental set-up: HJ heating jacket; HC heating coil; V Variac; TC thermocouple; TG temperature gauge; PED pyroelectric detector; LI lock-in amplifier; P plotter; M1 and M2 gold mirrors; W1 salt window (KCl); W2 quartz window; L1 and L2 salt lenses (KCl); QW quarter-wave plate (CdS); Ge germanium plate; PH iris pin hole

2.3. Experimental Arrangement

The experimental arrangement shown in Fig. 12 is similar to those used in previous studies on optically pumped parallel-plate DFB, single-helix HFB, and grazing-incidence DFB 496 μm CH_3F gas lasers [7–10, 12–14, 36, 60, 71, 72]. The pump laser is a hybrid CO_2 -laser (LSI-PRF150) with a linear polarization of the emission and tuned to the $9P(20)$ line at 9.55 μm wavelength. At the $9P(20)$ line, this laser produces pulse energies up to about 80 mJ for the TEM_{00} mode with a pulse duration of approximately 150 ns. This yields a maximum peak pulse power of the order of 500 kW. The infrared radiation emitted by this laser is guided through two mirrors M1 and M2 and fed into the 496 μm CH_3F -laser system through a potassium chloride (KCl) window W1.

Besides investigations with linearly polarized radiation, we have also performed experiments with circularly polarized pump radiation. For this purpose, we put a cadmium sulfide (CdS) quarter-wave plate QW into the CO_2 -laser pump beam and replaced the Brewster-angle mount of the KCl window by a mount where the plane of the KCl window is almost perpendicular to the waveguide axis. In order to assure that only the 496 μm CH_3F -laser radiation reaches the pyroelectric detector PED (ELTEC Instruments, Model 406), the laser system is equipped with a FIR transparent quartz window W2 to block the nonabsorbed fraction of the 9.55 μm CO_2 -laser pump beam after one pass through the laser waveguide. In order to reduce external noise on the detected signal, we apply a lock-in amplifier LI (Stanford Research Systems – SR 510) locked to the trigger frequency of the 9.55 μm

CO_2 -laser. With this technique, we have the possibility to average over a number of detected 496 μm laser pulses. The output signal from the lock-in amplifier is recorded on a plotter P as a function of the waveguide temperature T . In Fig. 12, the heating jacket mentioned in the previous Sect. 2.2 is denoted by HJ. It is a closed double-wall quartz cylinder which is mounted stressless and vacuum-sealed in a jig. In order to avoid stress during heating, one side of the jig is freely movable on guide bars parallel to the cylinder axis. The temperature control uses as sensor a chromel-alumel thermocouple TC attached to one end of the waveguide. A laboratory-made temperature gauge TG converts the thermoelectric voltage into degrees centigrade with an accuracy of better than $\Delta T = \pm 1^\circ\text{C}$ over the tuning range. Relevant for our measurements is that the recorded spectra are not affected by disturbing external resonator effects caused by reflections between the detector and the waveguide. By arranging the detector and the quartz window in a skew direction to the waveguide axis, as indicated in Fig. 12, and by a convex cut of the waveguide end on the output side, we have limited the influence of these effects on the measured resonances to less than 5%. For the beam alignment, we have applied a HeNe laser aligned collinear to the pump beam with the aid of a plane parallel germanium plate Ge. Also shown in Fig. 12 is an iris pin hole PH and a telescope lens system L1 and L2 for the variation of the cross-sectional energy density of the 9.55 μm CO_2 -laser pump beam.

2.4. Experimental Procedure

Although our CO_2 pump laser is equipped with an invar-stabilized internal-resonator mount, we have observed several irregularities which cause instable mode operation and beam disadjustment during warm-up. After about 30 min of continuous operation at a repetition frequency of 10 Hz, which corresponds to the recording conditions of the presented spectra, the CO_2 laser proved to be stable with an energy-output fluctuation less than $\Delta E = \pm 2\%$ over more than 1 h. This corresponds to the duration of one temperature scan of our mode spectra. In order to control the temporal shape of the laser beam, we used a photon drag detector which is inserted occasionally into the pump beam to verify the single-longitudinal-mode operation. The spatially stable CO_2 beam with a Gaussian intensity profile is then aligned collinear with the waveguide axis by application of a set of pin holes and a graphite foil. For the fine adjustment, we use the background fluorescence at room temperature to determine the optimal pump direction. We have also performed several experiments with the pump beam entering the CH_3F -laser system under a small angle of

about 10° relative to the waveguide axis. This changes the pump condition. Fortunately, it does not cause any principal change in the measured spectra. Only the output power of the observed resonances decreases due to the reduced illumination of the laser gas CH_3F . A total reproducibility of the $496\ \mu\text{m}$ output power for the different detected resonant modes could not be achieved, even though all measurable parameters such as pump energy, pump polarization, beam profile, and CH_3F gas pressure were held constant. One reason for this failure is the narrow $9.55\ \mu\text{m}$ absorption of the CH_3F and the displacement of this line relative to the center of the CO_2 -laser pump line [68]. As a result, a small shift in the CO_2 pump laser frequency due to an instable resonator length reduces the pump efficiency. With the output coupler of the CO_2 pump laser attached to a set of piezo crystals, we have tuned the resonator length by maintaining the single-longitudinal-mode operation. Thus, we registered a change of the output power by more than a factor 2, with as well as without focusing the pump beam into the CH_3F -laser waveguide. Another possible explanation of the poor reproducibility of the output power of the $496\ \mu\text{m}$ CH_3F laser may be the slightly inhomogeneous temperature distribution over the waveguide length as discussed in Sect.2.2. In particular for couplings with large coupling constants κ which yield high resonance densities on the temperature axis, or for an overlap between resonances belonging to different two-mode couplings, mode suppression and/or mode competition appears and results in output instabilities even for a small temperature variation over the waveguide. We have also registered influences of the pump mechanism. With the telescope lens system mentioned in Sect.2.3 which generates a higher $9.55\ \mu\text{m}$ energy density on the CH_3F -laser waveguide axis in addition to a significant gradient on the energy-density distribution over the waveguide cross section, the output power of the observed $496\ \mu\text{m}$ resonant modes shows a stronger fluctuation between different measurements than in the case when the pump beam is unfocused. Besides, the optical noise on the spectra diminishes with increasing homogeneity of the energy-density distribution of the CO_2 -laser pump beam. In order to achieve highest possible reproducibility, we frequently pumped the waveguide $496\ \mu\text{m}$ CH_3F -laser without the beam-contracting lens system.

Since measurements with different polarization states of the pump beam for both DFB and HFB waveguides have shown no changes in the mode spectra as far as the resonant temperatures are concerned, we generally applied linearly polarized $9.55\ \mu\text{m}$ pump radiation. All presented spectra refer to this polarization state. Yet, we have shown that the influence of the pump polarization on the output power

varies among different resonant modes. Therefore, we present measurements on the polarization dependence of selected strong resonant modes in DFB and HFB laser waveguides in the last Sect. 2.8.

In order to show all detected resonant modes for each waveguide geometry, we present combinations of the results from different temperature scans made with the same waveguide and under equivalent conditions. With respect to the difficult questions concerning output power of optically pumped standard DFB and HFB gas lasers, we renounce to list the output power of our detected resonant modes as quantitative data. Thus, the figures on the vertical axes of the presented mode spectra denoting the relative output power are merely quantitative measures and serve for an approximate comparison of the DFB and HFB mode characteristics of different waveguides and symmetries. Yet the average measured output power of our CH_3F $496\ \mu\text{m}$ laser emissions is estimated to be of the order of $200\ \text{W}$, whilst the maximum detected output power reached several kilowatts.

2.5. Measurements on DFB Waveguide $496\ \mu\text{m}$ CH_3F Lasers

In Figs. 13 to 16, we show the results of the measurements performed on $496\ \mu\text{m}$ CH_3F lasers equipped with periodic waveguides of different corrugation periods L . The waveguide parameters are listed in the figures. When comparing qualitatively the peaks in Figs. 13 to 15 with those in Fig. 16, we find that the halfwidth of a single resonance of the waveguides with $L \leq 248.0\ \mu\text{m}$ is less by a factor of about four than that of the waveguide with $L = 252.0\ \mu\text{m}$. This indicates that for the waveguides with $L \leq 248.0\ \mu\text{m}$, the observed couplings are stronger than the couplings responsible

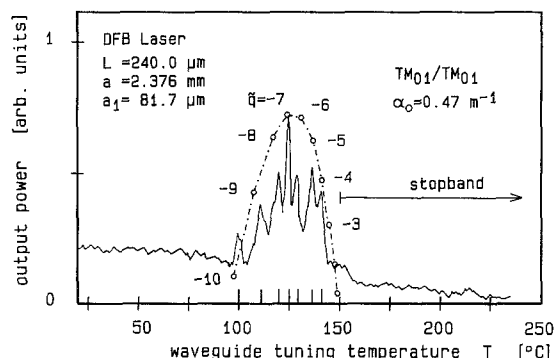


Fig. 13. Resonance spectrum of a DFB laser with a periodic waveguide of corrugation period $L = 240.0\ \mu\text{m}$, mean radius $a = 2.376\ \text{mm}$, and first Fourier coefficient $a_1 = 81.7\ \mu\text{m}$. The open circles (\circ) on the dash-dotted saturation curve indicate the calculated output powers and resonance temperatures for the lowest longitudinal modes below the lower stopband edge of the $\text{TM}_{01}/\text{TM}_{01}$ coupling for the small-signal gain $\alpha_0 = 0.47\ \text{m}^{-1}$

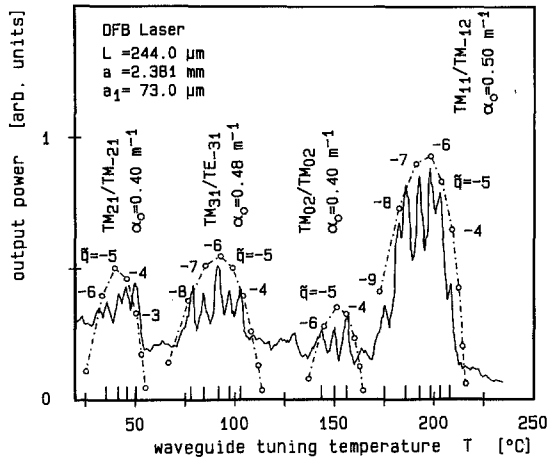


Fig. 14. Resonance spectrum of a DFB laser with a periodic waveguide of corrugation period $L=244.0\ \mu\text{m}$, mean radius $a=2.381\ \text{mm}$, and first Fourier coefficient $a_1=73.0\ \mu\text{m}$. The open circles (\circ) on the dash-dotted saturation curves indicate the calculated output powers and resonance temperatures for the lowest longitudinal modes below the stopband edge of the $\text{TM}_{21}/\text{TM}_{-21}$, $\text{TM}_{31}/\text{TE}_{-31}$, $\text{TM}_{02}/\text{TM}_{02}$, and $\text{TM}_{11}/\text{TM}_{-12}$ couplings. For the best envelope fits, we used the small-signal gains $\alpha_0=0.40\ \text{m}^{-1}$, $\alpha_0=0.48\ \text{m}^{-1}$, $\alpha_0=0.40\ \text{m}^{-1}$, and $\alpha_0=0.50\ \text{m}^{-1}$

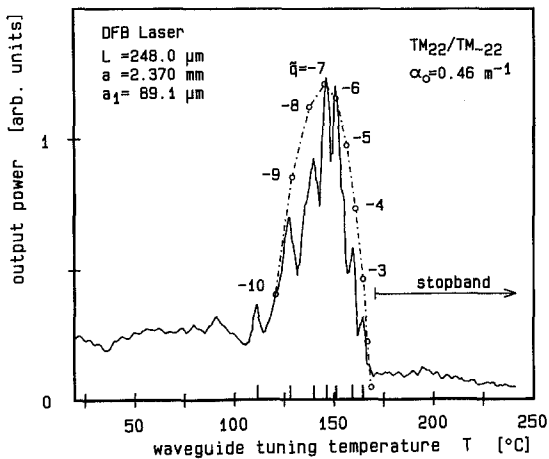


Fig. 15. Resonance spectrum of a DFB laser with a periodic waveguide of corrugation period $L=248.0\ \mu\text{m}$, mean radius $a=2.370\ \text{mm}$, and first Fourier coefficient $a_1=89.1\ \mu\text{m}$. The open circles (\circ) on the dash-dotted saturation curve indicate the calculated output powers and the resonance temperatures for the lowest longitudinal modes below the lower stopband edge of the $\text{TM}_{22}/\text{TM}_{-22}$ coupling for the small-signal gain $\alpha_0=0.46\ \text{m}^{-1}$

for the resonant modes of the waveguide with $L=252.0\ \mu\text{m}$. This conclusion is based on the rule that the stronger the coupling the more perfect the “distributed resonator mirrors”. Their performance is determined by the waveguide corrugation and by the increase of the quality factor for the DFB or HFB laser waveguide for increasing coupling strength [46]. Since,

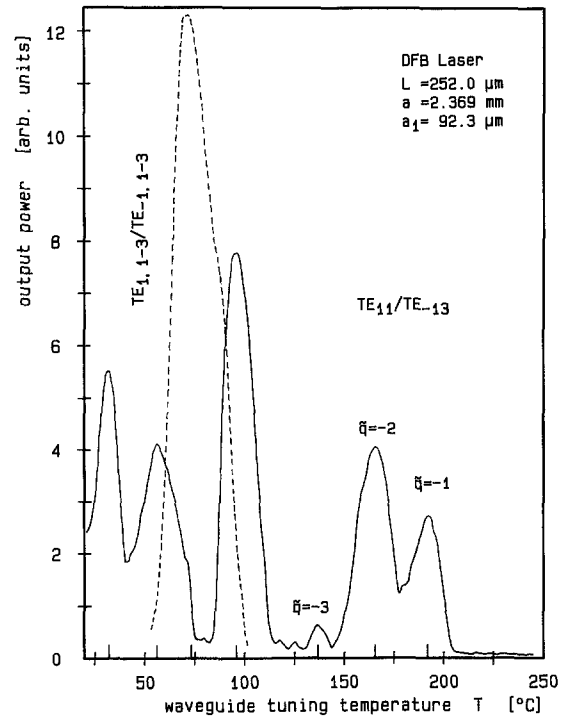


Fig. 16. Resonance spectrum of a DFB laser with a periodic waveguide of corrugation period $L=252.0\ \mu\text{m}$, mean radius $a=2.369\ \text{mm}$, and first Fourier coefficient $a_1=92.3\ \mu\text{m}$. The four leftmost peaks are identified with quasi two-mode resonances of the multi-mode coupling between TE modes belonging to the $m_+=1$ and $m_-=-1$ sets of modes (cf. Fig. 5), while the three at higher resonance temperatures represent the three lowest longitudinal modes below the lower stopband edge of the $\text{TE}_{11}/\text{TE}_{-13}$ coupling

in addition, the threshold gains for strong coupling are considerably lower than for weak coupling, this case is characterized by a high field intensity inside the waveguide which gives rise to gain saturation (cf. Sect. 1.8). In addition, the approximation $|k| \gg \alpha^{\text{th},L}$ which is the basis of the equation (67) for the resonance lengths $L_{\bar{q}}$ is valid and can, therefore, be used to identify the mode couplings.

Beginning with the periodic waveguide with period $L=240.0\ \mu\text{m}$, we find for the measured corrugation parameters when taking into account the selection rule (48) that the only two-mode coupling with stopband edge in the tuning range of interest is the lowest pure TM/TM coupling. For a Fourier coefficient slightly modified according to the uncertainty mentioned in Sect. 2.4 and the nonlinear thermal expansion described by (84), the lowest stopband edge for the $\text{TM}_{01}/\text{TM}_{01}$ coupling is located at $T=149^\circ\text{C}$. The dash-dotted envelope of the measured spectrum indicates the relative output power evaluated from the approximate saturation theory by Haus [63], (79), for consecutive longitudinal modes \bar{q} , which are indicated

by open circles. The best fit is obtained for a small-signal gain $\alpha_0 = 0.47 \text{ m}^{-1}$. The qualitative agreement between experiment and theory is striking for the lowest modes $|\tilde{q}| \leq 10$. The resonance \tilde{q}_{opt} with the strongest output is identified as $\tilde{q}_{\text{opt}} = -7$ from the measured data. Its half width FWHM is about $\Delta T \simeq 5^\circ\text{C}$ corresponding to a frequency bandwidth of $\Delta \nu \simeq 60 \text{ MHz}$.

The results of the second periodic waveguide illustrated in Fig. 14 show four different couplings with lower stopband edges within the tuning range. From the solution of the resonance condition (62), however, there is an additional fifth two-mode coupling to be expected. If we start with the coupling at the lowest resonance temperature, these five couplings are: $\text{TM}_{21}/\text{TM}_{-21}$ at $T = 55^\circ\text{C}$, $\text{TM}_{31}/\text{TE}_{-31}$ at $T = 114^\circ\text{C}$, $\text{TM}_{11}/\text{TE}_{-11}$ at $T = 122^\circ\text{C}$, $\text{TM}_{02}/\text{TM}_{02}$ at $T = 165^\circ\text{C}$, and $\text{TM}_{11}/\text{TM}_{-12}$ at $T = 218^\circ\text{C}$. If we compare these calculated couplings with the measured mode spectra, we find that the $\text{TM}_{11}/\text{TE}_{-11}$ coupling is missing. This absence can be explained by the fact that both the $\text{TM}_{31}/\text{TE}_{-31}$ and the missing coupling $\text{TM}_{11}/\text{TE}_{-11}$ have approximately the same interaction range, i.e. $T \simeq 70^\circ\text{C}$ to 120°C . Since, moreover, the ratio between the strengths $|\kappa|$ of these couplings is about 1.6:1.0, the $\text{TM}_{31}/\text{TE}_{-31}$ coupling is favoured. Therefore, the $\text{TM}_{11}/\text{TE}_{-11}$ coupling may be suppressed. All remaining couplings have about the same coupling strength $|\kappa| \lesssim 400 \text{ m}^{-1}$, which is almost as large as that of the $\text{TM}_{01}/\text{TM}_{01}$ coupling in the previously discussed waveguide (Fig. 13). Consequently, also the bandwidths of all these resonant modes are almost identical, i.e. $\Delta \nu \simeq 70 \text{ MHz}$. As before, the dash-dotted envelopes in Fig. 14 represent the theoretical output power fitted to the experimental data. For these fits, we used the small-signal gains $\alpha_0 = 0.40 \text{ m}^{-1}$, $\alpha_0 = 0.48 \text{ m}^{-1}$, $\alpha_0 = 0.40 \text{ m}^{-1}$, and $\alpha_0 = 0.50 \text{ m}^{-1}$ for the four observed couplings.

For the periodic waveguide with period $L = 248.0 \mu\text{m}$ (Fig. 15), we again find only one two-mode coupling with the interaction range inside the tuning range. The calculated lower stopband edge at $T \simeq 175^\circ\text{C}$ as well as the coupling strength $|\kappa| \simeq 475 \text{ m}^{-1}$ of this $\text{TM}_{22}/\text{TM}_{-22}$ coupling indicate that the set of observed resonant modes can be assigned to this coupling with high certainty. The excellent fit of the output-power envelope for the small-signal gain $\alpha_0 = 0.47 \text{ m}^{-1}$ as well as the agreement between measured and calculated resonance temperatures also prove the identification of the coupling.

For the periodic waveguide with period $L = 252.0 \mu\text{m}$ (Fig. 16), the theory predicts five different two-mode couplings with azimuthal mode numbers $|m| \leq 5$ and stopband edges somewhere in the temperature range between room temperature and $T = 250^\circ\text{C}$.

However, taking the mode separation and the width of the measured resonances as criterions, the two strong couplings $\text{TM}_{11}/\text{TM}_{-14}$ and $\text{TE}_{11}/\text{TE}_{-11}$ have to be rejected. Comparing the resonance temperatures of the experimental spectrum with those of the theoretical spectrum, we find the strongest of the remaining couplings, i.e. the $\text{TE}_{11}/\text{TE}_{-13}$ coupling with $|\kappa| \simeq 31 \text{ m}^{-1}$ and with the lower stopband edge just below $T = 200^\circ\text{C}$, to fit the three resonant modes at $T = 137^\circ\text{C}$, $T = 167^\circ\text{C}$, and $T = 190^\circ\text{C}$. In this case, however, we have to allow for variations of the resonance temperatures of $\Delta T \simeq \pm 3^\circ\text{C}$ between different scans.

The four resonances observed at resonance temperatures below $T = 100^\circ\text{C}$ show a phenomenon observed for many of the investigated waveguides. If the theoretical resonance density is equal or less than the measured width of two neighbouring resonances, it may occur that a new resonance appears followed by an almost total suppression of the two neighbouring resonances. We mark these rarely observed resonances as dashed peaks. A plausible explanation is the slight variation of the temperature over the waveguide, which reduces the resolution power and simultaneously favours mode competition (cf. Sect. 2.2).

In order to identify the observed resonances in the temperature range below $T = 100^\circ\text{C}$, we first consider the two remaining weak couplings $\text{TE}_{01}/\text{TE}_{02}$ and $\text{TE}_{12}/\text{TE}_{-12}$. Since both are very weak ($|\kappa| < 10 \text{ m}^{-1}$), high threshold gains occur even for the lowest longitudinal modes $|\tilde{q}| = 1$. A comparison between experimental and theoretical resonance temperatures of these couplings shows that the mode with the lowest threshold gain, i.e. the $\tilde{q} = +1$ mode of the $\text{TE}_{12}/\text{TE}_{-12}$ coupling, explains well the observed resonance at $T = 96^\circ\text{C}$. The other resonant peaks, however, cannot be explained by the two-mode coupling theory. Therefore, we have applied the extended multi-mode theory outlined in Sect. 1. Although the multi-mode couplings are in general suppressed by two-mode couplings, multi-mode resonant modes can arise under certain conditions. They are observed when there is a number of overlapping, relatively weak two-mode couplings in the vicinity of the tuning range. In the waveguide considered, there are two weak couplings of the $m_+ = 1$ and $m_- = -1$ sets of modes. Hence, a multi-mode coupling can dominate. The waveguide parameters used for the contour plot Fig. 4 are identical with those of the waveguide under consideration. If we compare the measured spectrum of Fig. 16 with the calculated resonances of the $\text{TE}_{1,1-3}/\text{TE}_{-1,1-3}$ multi-mode coupling, we find a good agreement for all the four resonant modes below $T = 100^\circ\text{C}$. The small temperature shifts are assumed to originate in the strong sensitivity of multi-mode

resonance temperatures and threshold gains on additional modes of the two considered sets of modes m_+ and m_- . Whether the calculated multi-mode resonance at about $T=96^\circ\text{C}$ is identical with the observed resonance or whether it originates in the previously investigated $\text{TE}_{12}/\text{TE}_{-12}$ coupling cannot be decided definitely. In both cases, the threshold gain is of the same order of magnitude.

2.6. Measurements on Single-Helix HFB Waveguide 496 μm CH_3F Lasers

The geometrical parameters of the two helical waveguides whose mode spectra are presented in Figs.17 and 18 allow us to make temperature scans in a region full of potential two-mode couplings, as for the DFB waveguide with corrugation period $L=252.0\mu\text{m}$. From the character of the observed resonant modes and with the experience from the interpretation of the previously shown resonances of high output power, we presume that also here we are primarily dealing with moderate couplings basically containing TE modes.

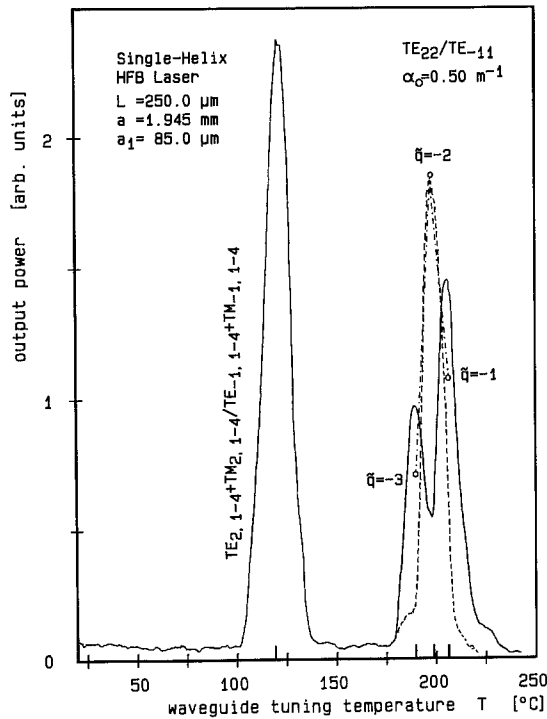


Fig. 17. Resonance spectrum of an HFB laser with a single-helix waveguide of corrugation pitch $L=250.0\mu\text{m}$, mean radius $a=1.945\text{mm}$, and first Fourier coefficient $a_1=85.0\mu\text{m}$. The strong single resonance at $T=119^\circ\text{C}$ is identified with a frustrated intrastopband mode of the multi-mode coupling between TE and TM modes belonging to the $m_+=2$ and $m_-=-1$ sets of modes, while the three at higher resonance temperatures represent the three lowest longitudinal modes below the lower stopband edge of the $\text{TE}_{22}/\text{TE}_{-11}$ coupling fitted with the small-signal gain $\alpha_0=0.50\text{m}^{-1}$ (○)

For the waveguide with pitch $L=250.0\mu\text{m}$ and oversize factor $f\simeq 8$, we find that the $\text{TE}_{22}/\text{TE}_{-11}$ coupling with a theoretical lower stopband edge at $T=212^\circ\text{C}$ explains the set of resonances around $T=200^\circ\text{C}$ (Fig. 17). If we assume the dashed resonance to represent the $\bar{q}=-2$ mode, the resonance separation for this coupling fits the theory indicated by open circles which also mark the calculated power of the saturated output. This fit has been performed with the small-signal gain $\alpha_0=0.50\text{m}^{-1}$. The observed strong variation of the output in this range can, except for internal mode competition, be related to another slightly stronger coupling which also involves the TE_{-11} mode. Furthermore, these two couplings are characterized by almost identical lower stopband edges. These observations, together with the fact that three further two-mode couplings including modes belonging to the $m_+=2$ and $m_-=-1$ sets of modes have interaction regions in the neighbourhood, justify the assumption of a multi-mode coupling. The numerical evaluation of the corresponding

$$\text{TE}_{2,1-4} + \text{TM}_{2,1-4} / \text{TE}_{-1,1-4} + \text{TM}_{-1,1-4}$$

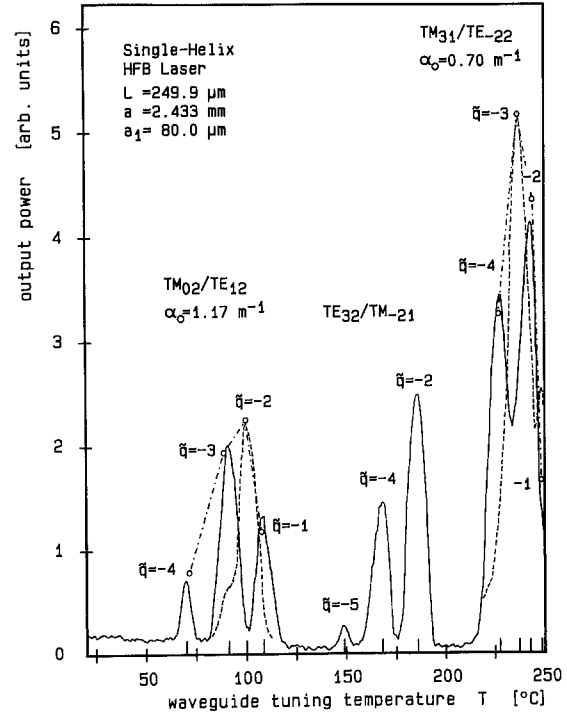


Fig. 18. Resonance spectrum of an HFB laser with a single-helix waveguide of corrugation pitch $L=249.9\mu\text{m}$, mean radius $a=2.433\text{mm}$, and first Fourier coefficient $a_1=80.0\mu\text{m}$. The open circles (○) on the dash-dotted saturation curves for the two outer sets of modes indicate the calculated output power and the resonance temperatures for the lowest longitudinal modes below the lower stopband edge of the $\text{TM}_{02}/\text{TE}_{12}$ and $\text{TM}_{31}/\text{TE}_{-22}$ mode couplings. For the best envelope fit, we used the small-signal gains $\alpha_0=1.17\text{m}^{-1}$ and $\alpha_0=0.70\text{m}^{-1}$. The resonances in the center are identified with the $\text{TE}_{32}/\text{TM}_{-21}$ coupling

coupling predicts a frustrated intrastopband multimode resonance just below $T=120^\circ\text{C}$ in consistence with the measured spectrum. Since on one hand, there are no indications of a split of this observed resonance and on the other hand, there are no weak two-mode couplings present in the tuning range, we suggest this resonance to result from the mentioned multi-mode coupling.

The experimental mode spectrum of the waveguide with pitch $L=249.9\ \mu\text{m}$ and oversize factor $f \simeq 10$ is shown in Fig. 18. The geometry of this waveguide corresponds approximately to that used by Preiswerk et al. [12–14] for the first realization of the HFB gas laser with the difference that the corrugation of the discussed waveguide is cut with another screw tap. In contrast to the single resonance observed by Preiswerk et al. [12–14], we detect a large number of resonances distributed over the entire tuning range. Correspondingly, measurements on various waveguides with officially identical geometry have shown a strong variation in the detected mode spectra. From the experimental point of view, it seems that the coupling responsible for the resonant modes around $T=100^\circ\text{C}$ occurs easily, whilst the set of resonances in the center of the spectra was found to be the most critical. For all investigated waveguides, we observed at least one resonance near $T=100^\circ\text{C}$, yet only for the waveguide discussed here, all the resonances of Fig. 18 were observed.

The mode competition in the temperature tuning range below $T=110^\circ\text{C}$ gives rise to one instable resonance (dashed peak) located at $T=100^\circ\text{C}$. Under the assumption that this peak represents a true resonant mode, the comparison between experiment and two-mode coupling theory for the $\text{TM}_{02}/\text{TE}_{12}$ coupling gives good agreement for all four observed resonances in this range. For the best fit of the output power, we used the small-signal gain $\alpha_0 = 1.17\ \text{m}^{-1}$. In the temperature range from $T=150^\circ\text{C}$ to 200°C , the mode competition between the resonant modes is stronger than at lower temperatures. This serves as an indication of a higher resonance density, equivalent to a stronger coupling. Correspondingly, we assign the observed resonant modes to various longitudinal modes of the $\text{TE}_{32}/\text{TM}_{-21}$ coupling which is about twice as strong as the $\text{TM}_{02}/\text{TE}_{12}$ coupling and exhibits a lower stopband edge at $T=190^\circ\text{C}$. In contrast to the resonances near $T=100^\circ\text{C}$, the three lowest longitudinal modes centered around the mode at $T=186^\circ\text{C}$ show a mode competition which does not exhibit distinct resonances at shifted temperatures, yet a more or less well-defined broadening of the main resonance $\tilde{q} = -2$. For this reason, not all longitudinal modes expected are present in Fig. 18 but only those with distinct peaks. We assume that the observed

feature of this mode coupling has its origin in the previously mentioned difficulties in exciting the coupling.

Finally, the split strong resonant modes occurring above $T=225^\circ\text{C}$ are identified with the $\text{TM}_{31}/\text{TE}_{-22}$ coupling with the lower stopband edge at $T=249^\circ\text{C}$. The observed mode separation for the four lowest longitudinal modes at the lower stopband edge of this coupling once more coincides to a high extent with the calculated resonant tuning temperatures. The estimated output power for these four modes with a small-signal gain $\alpha_0 = 0.70\ \text{m}^{-1}$ also agrees well with our experiment. In order to verify the calculated lower stopband edge, we extended the temperature tuning range to $T=275^\circ\text{C}$ without observing additional resonances.

Measurements on a helical waveguide with oversize factor $f \simeq 6$ show without exception only a weak superradiation from the CH_3F -laser gas. According to theory, the corrugation parameters promise two stopband edges within the temperature tuning range. Both couplings, however, are almost twice as strong as the observed strong couplings in the DFB waveguides of Figs. 13–15. Consequently, the virtual resonator mirrors of the corrugated waveguide become practically perfect and the mode couplings only cause a build-up of an internal field without allowing for any output. On the other hand, we detect many resonances homogeneously distributed over the temperature tuning range for a waveguide with oversize factor $f \simeq 12$. Due to the large number of either weak or strong couplings with an interaction region in this range, no definite identification of resonant modes can be performed. None of the resonances, however, reaches the output power of the strongest modes detected in the other single-helix HFB waveguides.

2.7. Measurements on Double-Helix HFB Waveguide $496\ \mu\text{m}$ CH_3F Lasers

For the first time, we have achieved laser action with hollow corrugated metal waveguides with the symmetry of the double helix as feedback devices. Figure 19 shows the measured mode spectrum of a waveguide with pitch $2L=499.8\ \mu\text{m}$ and oversize factor $f \simeq 8$. As expected for the temperature range below $T=170^\circ\text{C}$ where the observed resonance density is high, the mode competition in this region is strong. As a consequence, the presented spectrum is therefore a combination of different scans. In contrast, the two rightmost broad resonances are both reproduced unaltered from scan to scan. This indicates that we in the upper tuning range are dealing with an effectively high mode separation as a result of a weak coupling.

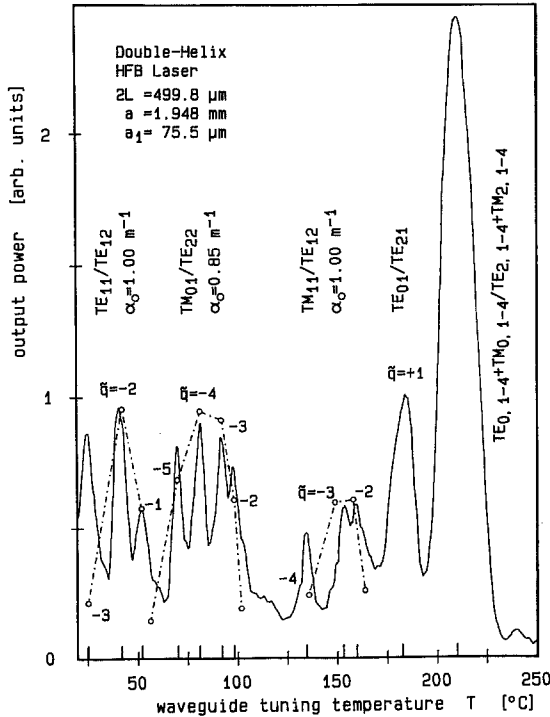


Fig. 19. Resonance spectrum of an HFB laser with a double-helix waveguide of corrugation pitch $2L=499.8\mu\text{m}$, mean radius $a=1.948\text{ mm}$, and first Fourier coefficient $a_1=75.5\mu\text{m}$. The open circles (o) on the dash-dotted saturation curves indicate the calculated output powers and resonance temperatures for the lowest longitudinal modes below the lower stopband edge of the $\text{TE}_{11}/\text{TE}_{12}$, $\text{TM}_{01}/\text{TE}_{22}$, and $\text{TM}_{11}/\text{TE}_{12}$ couplings. For the best envelope fit, we used the small-signal gains $\alpha_0=1.00\text{ m}^{-1}$, $\alpha_0=0.85\text{ m}^{-1}$, and $\alpha_0=1.00\text{ m}^{-1}$. The first of the two remaining resonances is identified with the first longitudinal mode above the upper stopband edge of the $\text{TE}_{01}/\text{TE}_{21}$ coupling, and the one at highest resonance temperature represents a frustrated intrastopband mode of the multi-mode coupling between TE and TM modes belonging to the $m_+=0$ and $m_-=2$ sets of modes (cf. Fig. 6)

The identification of the observed resonances can be performed similar to that of the DFB and the single-helix HFB waveguides. The only basic difference is that we now have to apply the chirality factor $\bar{m}=2$ for a right-handed double helix in the selection rule (48) for the selection of the possible two-mode couplings. From the calculation of all resonance temperatures within the spectral window investigated, we can identify the three resonances at the lowest temperatures with the first three longitudinal modes at the lower stopband edge of the $\text{TE}_{11}/\text{TE}_{12}$ coupling. The next set of four distinct resonances can be assigned with the same accuracy to the $\text{TM}_{01}/\text{TE}_{22}$ coupling which has its lower stopband edge at $T=104^\circ\text{C}$. Since its coupling strength is twice that of the previous coupling, its spectrum is denser. The three following resonances between $T=134^\circ\text{C}$ and $T=160^\circ\text{C}$ in Fig. 19 can be

identified with the $\text{TM}_{11}/\text{TE}_{12}$ coupling which is the only one with an interaction region in this temperature range. Its lower stopband edge is located at $T=167^\circ\text{C}$, whilst its coupling strength is between those calculated for the previous two couplings.

In analogy to the spectra presented for DFB-laser waveguides, the dash-dotted envelopes represent the normalized output power according to (79) fitted to the experimental data. The circles denote the theoretical resonance temperatures which have to be compared with the experimental resonances indicated by the hatches on the temperature axis. Again, the qualitative reproduction of the power characteristics and the striking agreement between experimental and theoretical resonance temperatures are remarkable. The output-power fits are calculated for the three couplings with the small-signal gains $\alpha_0=1.00\text{ m}^{-1}$, $\alpha_0=0.85\text{ m}^{-1}$, and $\alpha_0=1.00\text{ m}^{-1}$.

Finally, we observe in Fig. 19 that the resonant modes at $T=183^\circ\text{C}$ and $T=210^\circ\text{C}$ are more than twice as broad as the other resonances of this waveguide, which implies that their origins are either weak two-mode couplings or multi-mode couplings. In agreement with this assumption, we find that the only weak coupling at hand, i.e. the $\text{TE}_{01}/\text{TE}_{21}$ coupling, has its first longitudinal mode $\bar{q}=+1$ above the stopband at $T=181.5^\circ\text{C}$. The next longitudinal mode $\bar{q}=+2$ of this coupling is located at $T=213^\circ\text{C}$. Since the threshold gain of this mode exceeds the maximum gain of the CH_3F gas at $496.1\mu\text{m}$ [73], we doubt, however, that this mode can oscillate. Instead, we postulate a frustrated stopband mode of the multi-mode coupling between the sets of modes $m_+=0$ and $m_-=2$ as an explanation of the observed resonance at $T=210^\circ\text{C}$. The contour plot of the theoretical evaluation of the determinant of the transmission matrix (59) for this multi-mode coupling which includes eight forward and eight backward propagating modes is shown in Fig. 5. As shown, the resonance at $T=208^\circ\text{C}$, which has the lowest threshold gain, fits well with the measured peak. Since its threshold gain is slightly less than that for the $\bar{q}=+1$ of the $\text{TE}_{01}/\text{TE}_{21}$ coupling, the difference in output power between these two broad resonances can be explained as well.

Double-helix HFB resonances have also been observed for a $496\mu\text{m}$ laser with a waveguide of oversize factor $f \simeq 10$. The resulting spectrum is shown in Fig. 20. Instead of combining different scans in order to avoid smearing out of resonances due to mode competition, we have represented the rarely oscillating resonances by dashed lines as in Figs. 16–18. For the waveguide with the parameters indicated in Fig. 20, we find three two-mode couplings which match the measured spectrum. The experimental resonance temperatures for the four resonances below $T=75^\circ\text{C}$

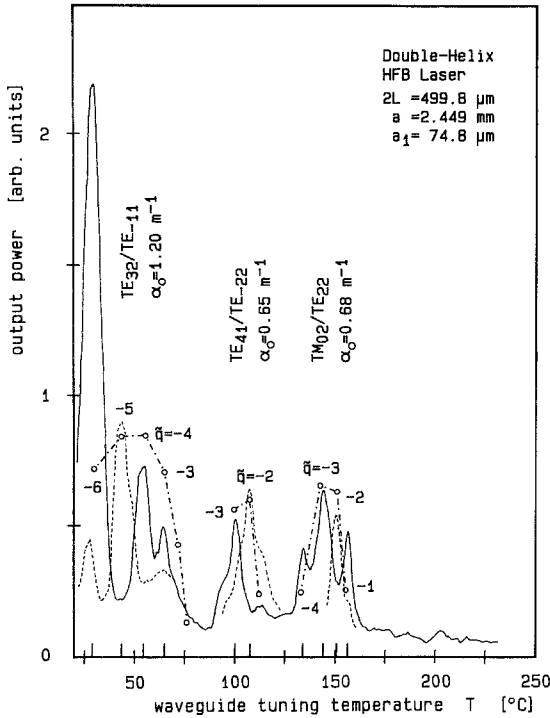


Fig. 20. Resonance spectrum of an HFB-laser with a double-helix waveguide of corrugation pitch $2L=499.8\ \mu\text{m}$, mean radius $a=2.449\ \text{mm}$, and $a_1=74.8\ \mu\text{m}$. The open circles (o) on the dash-dotted saturation curves indicate the calculated output powers and resonance temperatures for the lowest longitudinal modes below the lower stopband edge of the $\text{TE}_{32}/\text{TM}_{-11}$, $\text{TE}_{41}/\text{TE}_{-22}$, and $\text{TM}_{02}/\text{TE}_{22}$ couplings. For the best envelope fits, we used the small-signal gains $\alpha_0=1.20\ \text{m}^{-1}$, $\alpha_0=0.65\ \text{m}^{-1}$, and $\alpha_0=0.68\ \text{m}^{-1}$

agree well with the $\text{TE}_{32}/\text{TM}_{-11}$ coupling as indicated by the open circles of the dash-dotted power envelope fitted with the small-signal gain $\alpha_0=1.20\ \text{m}^{-1}$. An interesting feature of Fig. 20 is the output power of mode $\tilde{q}=-6$, which is considerably stronger than that of mode $\tilde{q}=-5$. An explanation may be the slightly inhomogeneous temperature distribution over the waveguide length above room temperature. This implies a more efficient coupling at room temperature than at higher temperatures where the distribution of the corrugation pitch or period becomes broader. A similar, yet smaller deviation between saturation fit and measured spectrum is also observed for the $\tilde{q}=-3$ mode of the $\text{TE}_{11}/\text{TE}_{12}$ coupling at $T=25^\circ\text{C}$ in Fig. 19. With similar agreement between experimental and theoretical resonance temperatures, we can identify the residual observed resonances of this waveguide by the $\text{TE}_{41}/\text{TE}_{-22}$ and the $\text{TM}_{02}/\text{TE}_{22}$ couplings with lower stopband edges at $T=113^\circ\text{C}$ and $T=157^\circ\text{C}$. For the output-power fits of these couplings, we have applied the small-signal gains $\alpha_0=0.65\ \text{m}^{-1}$ and $\alpha_0=0.68\ \text{m}^{-1}$.

2.8. Dependence of DFB and HFB Resonances on the Polarization of the Pump Radiation

In order to investigate the dependence of the FIR output power on the polarization state of the CO_2 -laser pump beam, we have applied an AR coated quarter-wave plate mounted in a holder which permits a continuous rotation around the direction of propagation of the pump beam. Furthermore, we have replaced the Brewster-angle mount on the pump side of the waveguide $496\ \mu\text{m}$ CH_3F laser by another mount with the salt window almost perpendicular to the beam. This serves to minimize the discrimination of different polarizations and simultaneously to avoid the formation of an external resonator (cf. Sect. 2.3).

A result of this kind of measurements is shown in Fig. 21. Here, the normalized output power for five resonant modes of the DFB-laser waveguide with period $L=252.0\ \mu\text{m}$ (Fig. 16) is shown for different rotation angles of the quarter-wave plate. As observed in the figure, a linearly polarized pump beam favours the resonances below $T=100^\circ\text{C}$, whilst the resonances at higher temperatures reach maxima for circularly polarized pump radiation. The influence of the polarization on the threshold condition for the different resonances is not covered by the coupled-wave theory described in Sect. 1. Nevertheless, it seems obvious that resonances belonging to the same coupling react similarly to a change in the pump polarization. Consequently, we can apply the pump-polarization measurements to confirm the identification of the resonances in the spectra. A comparison between different measurements at the same resonance shows that small changes in the operational conditions can cause a noticeable, yet not always reproducible variation of the magnitude of the minima observed for the curves in Fig. 21.

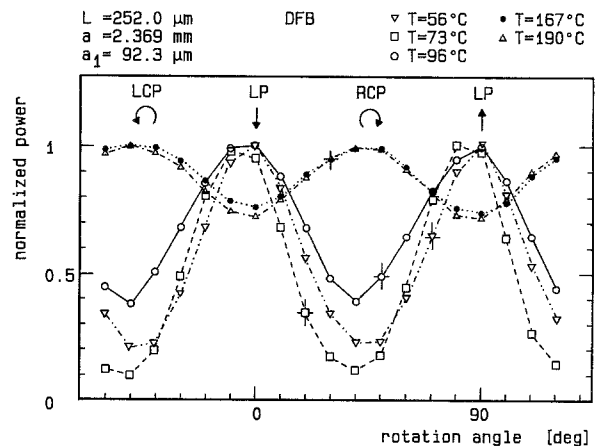


Fig. 21. Dependence of the FIR output power on the polarization state of the pump radiation for five different resonances of the DFB resonance spectrum shown in Fig. 16. The normalized output power is plotted versus the angle adjust of the quarter-wave plate

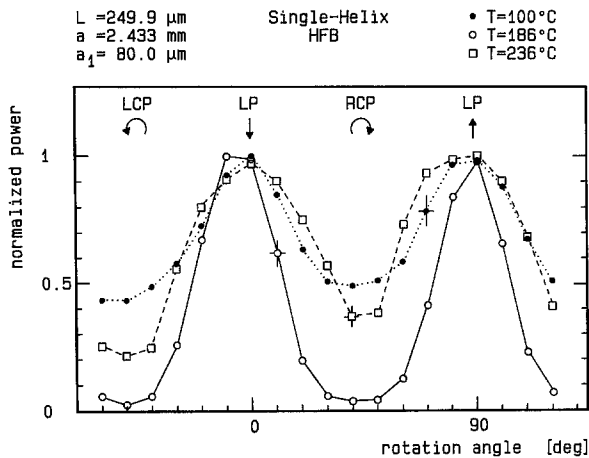


Fig. 22. Dependence of the FIR output power on the polarization state of the pump radiation for three different resonances of the single-helix HFB resonance spectrum shown in Fig. 18. The normalized output power is plotted versus the angle adjust of the quarter-wave plate

However, the angles corresponding to maximal and minimal output powers remain unchanged for a given resonance. This implies that these angles are specific for each coupling. The errors indicated by bars are due to variations occurring in each measurement. They do not include variations among different experimental surveys of a fixed resonance.

Experimental measurements on waveguides with helical symmetry showed similar characteristics with the difference that every investigated resonance shows a maximal output for linearly polarized pump radiation. In Fig. 22, the behaviour of one resonance of each set of resonances shown in Fig. 18 is illustrated. The total absence of the resonance at $T=186^\circ\text{C}$ for both circular polarization states is remarkable. Among all the investigated strong resonances, this is the only which exhibits such a strong dependence on the polarization of the pump radiation. It is difficult to determine whether the $\text{TE}_{32}/\text{TM}_{-21}$ coupling really implies a higher discrimination of circularly polarized pump radiation than the other observed couplings, or whether the observed effect is merely a result of a less efficient pumping. Since the maximum output powers for the $T=100^\circ\text{C}$ and the $T=186^\circ\text{C}$ resonances are approximately equal, it seems obvious, however, that the dependence on the polarization of the pump radiation plays a dominant role.

In contrast to the investigated DFB-laser waveguides, the right-handed HFB-laser waveguides show a weak, yet definite indication of a lower oscillation threshold for right-handed than for left-handed circular pump polarization. This implies that a proper theory of the observed features has to include the

polarization of the pump beam as well as the symmetry of the waveguide corrugation.

3. Conclusions

We have performed theoretical as well as experimental studies on circular oversized hollow periodic and helical metal waveguides used in DFB and HFB FIR gas lasers. These waveguides are tuned to the DFB and HFB resonances by thermal expansion.

The theoretical investigation is based on the coupled-wave theory, which was extended in order to allow for the coupling of an unlimited number of simultaneously counterrunning modes in the corrugated waveguide. In analogy to the derivation of the resonance condition in the scalar formalism of the two-mode coupling, we derived the corresponding resonance condition for the generalized multi-mode coupling in a matrix form. Moreover, both the transmission and the reflection matrix characteristic for the oversized periodic or helical waveguides were formulated. When the number of counterrunning modes is reduced to two, all expressions derived for the multi-mode coupling revert into those relevant for the two-mode coupling. This is a confirmation of the validity of our multi-mode extension. Our numerical investigations of the resonance condition have shown that the resonances of a multi-mode coupling can be divided into different categories depending on whether the individual two-mode couplings involved in the multi-mode coupling are interfering or not. On the first hand, in regions where the interaction between different couplings is weak, the calculated resonance spectrum is practically identical with that of the solution of the resonance condition of the simple two-mode coupling. On the other hand, resonances occurring in regions where various two-mode stopbands are either fully or partly overlapping cannot be compared with resonances of a two-mode coupling. The important feature of these resonances is that the threshold gains of these so-called frustrated intrastopband modes are considerably higher than the corresponding gains for pure two-mode couplings. Therefore, we conclude that the generation of a multi-mode resonance becomes suppressed in the presence of resonances originating in a pure two-mode coupling although the corrugated waveguide is strongly oversized. Oscillations due to multi-mode coupling are consequently only possible at frequencies, or temperatures, sufficiently far away from the stopband edges of the two-mode coupling.

In the experimental part of this study, we have measured the mode spectra of a large number of DFB and HFB gas lasers of different geometries. We have for the first time realized and investigated circular

symmetric waveguides with periodic wall corrugations and demonstrated operation of HFB lasers with the waveguide symmetry of the double helix. For HFB lasers with single-helix waveguides, we have succeeded in increasing the number of observed laser modes. The reproducibility of detected laser spectra for different waveguides with identical geometries within the frame of the manufacturing tolerances was found to be good as far as the position of the observed resonances is concerned. The output power of the individual laser modes, however, shows a strong variation from waveguide to waveguide. This fact is an indication for the assumption that the average waveguide parameters alone are responsible for the location of the resonances on the frequency or temperature axis, whilst small local deviations along the waveguide axis can affect the effective threshold gains of the laser modes.

The statement that the probability of a laser oscillation originating in a multi-mode coupling is low due to high threshold gains was experimentally verified. Almost all of the detected laser modes of the various investigated waveguides were identified with modes assigned to pure two-mode coupling. Those resonances, however, which could not be explained in terms of two-mode couplings were found to coincide well with calculated multi-mode couplings of low threshold gains. The good agreement between theoretical predictions and experimental observations concerning resonance temperatures and separations between consecutive longitudinal modes is a confirmation of the validity of the coupled-wave theory applied. It also manifests the accuracy of the overlap integral for the calculation of the coupling strengths and the selection rule for coupling modes in hollow metal waveguides with periodic or helical corrugations.

Although the linear coupled-wave theory in its usual form is found satisfactory for the interpretation of the observed resonance temperatures, it cannot be used to explain the observed output-power characteristics of the longitudinal modes in a strong coupling. In disagreement with the prediction of strongest output power at the stopband edges made under the assumption of a medium gain independent of intensity, we observed a shift of the maximum output power away from the stopband. This feature observed for the first time is explained by the introduction of a nonlinear gain into the coupled-wave equations in accordance with an approach by Haus [63] derived for strong coupling. The optimal longitudinal mode which exhibits the strongest output power is found theoretically as well as experimentally to vary with the coupling strength. In case of a sufficiently weak coupling, the effect of the saturation disappears as far as the output-

power is concerned. In this case, the output-power characteristics are described by the linear coupled-wave theory.

Acknowledgements. We are very grateful to H. Kogelnik and C. V. Shank, Holmdel, USA, and A. Müller, Göttingen, FRG, Z. Bor, Szeged, H, and P. Szczepanski, Warsaw, PL for valuable discussions and suggestions. Furthermore, we owe thanks to W. Herrmann, Zürich, F. Jäger, Brüttisellen, B. Grossmann, Zürich, D. Charpillot SA, Malleray, SIG, Neuhausen, and W. Flühmann AG, Dübendorf, for a great help with the manufacture of the periodic and helical waveguides.

This study was supported by the Swiss National Science Foundation, the Huber-Kudlich Foundation, and ETH Zürich.

References

1. H. Kogelnik, C.V. Shank: Appl. Phys. Lett. **18**, 152–154 (1971)
2. C.V. Shank, J.E. Bjorkholm, H. Kogelnik: Appl. Phys. Lett. **18**, 395–396 (1971)
3. H. Kogelnik, C.V. Shank: J. Appl. Phys. **43**, 2327–2335 (1972)
4. S. Gnepf, F.K. Kneubühl: Infr. mmWaves **16**, 35–76 (1986)
5. M. Nakamura, A. Yariv, H.W. Yen, S. Somekh, H.L. Garvin: Appl. Phys. Lett. **22**, 515–516 (1973)
6. D. Marcuse: IEEE J. QE-8, 661–669 (1972)
7. E. Affolter, F.K. Kneubühl: Phys. Lett. **74A**, 407–408 (1979)
8. F.K. Kneubühl, E. Affolter: J. Opt. **11**, 449–453 (1980)
9. E. Affolter, F.K. Kneubühl: IEEE J. QE-17, 1115–1122 (1981)
10. F.K. Kneubühl, E. Affolter: Infr. mmWaves **5**, 305–337 (1982)
11. K.O. Hill, Y. Fujii, D.C. Johnson, B.S. Kawasaki: Appl. Phys. Lett. **32**, 647–649 (1978)
12. H.P. Preiswerk, G. Küttel, F.K. Kneubühl: Phys. Lett. **93A**, 15–17 (1982)
13. H.P. Preiswerk, M. Lubanski, S. Gnepf, F.K. Kneubühl: IEEE J. QE-19, 1452–1457 (1983)
14. H.P. Preiswerk, M. Lubanski, F.K. Kneubühl: Appl. Phys. B **33**, 115–131 (1984)
15. Y. Itaya, T. Matsuoka, K. Kuroiwa, T. Ikegami: IEEE J. QE-20, 230–235 (1984)
16. K. Utaka, S. Akiba, K. Sakai, Y. Matsushima: IEEE J. QE-20, 236–245 (1984)
17. L.D. Westbrook, I.D. Henning, A.W. Nelson, P.J. Fiddymment: IEEE J. QE-21, 512–518 (1985)
18. F. Favre: IEEE J. QE-23, 81–88 (1987)
19. M. Yamada, K. Sakuda: J. Opt. Soc. Am. A **4**, 69–76 (1987)
20. M. Kuznetsov: IEEE J. QE-24, 1837–1844 (1988)
21. Y. Nakano, K. Tada: IEEE J. QE-24, 2017–2033 (1988)
22. T. Numai, S. Murata, I. Mito: Appl. Phys. Lett. **53**, 83–85 (1988)
23. H. Temkin, R.A. Logan, R.F. Karliceck, Jr., K.E. Strege, J.P. Blaha, P.M. Gabla, A. Savage, K. Oatis: Appl. Phys. Lett. **53**, 1156–1158 (1988)
24. T. Numai, S. Murata, I. Mito: Appl. Phys. Lett. **53**, 1168–1169 (1988)
25. P. Correc, N. Bouadma, J. Landreau: Opt. Commun. **65**, 433–436 (1988)
26. Z. Bor: IEEE J. QE-16, 517–528 (1980)
27. Z. Bor, A. Müller, B. Racz, F.P. Schäfer: Appl. Phys. B **27**, 9–14, 77–81 (1982)

28. K.E. Süsse: *Appl. Phys.* B **37**, 99–106 (1985)
29. Z. Bor, A. Müller: *IEEE J. QE*-**22**, 1524–1533 (1986)
30. J. Hebling, Z. Bor: *Opt. Acta* **33**, 1063–1071 (1986)
31. F. Raksi: *Appl. Phys.* B **47**, 91–96 (1988)
32. J. Hebling: *Appl. Phys.* B **47**, 267–272 (1988)
33. Szatmári, F.P. Schäfer: *Appl. Phys.* B **47**, 305–311 (1988)
34. F.K. Kneubühl: *Rev. Roumaine Phys.* **33**, 691–703 (1988)
35. F.K. Kneubühl, M.W. Sigrist: *Laser* (Teubner, Stuttgart 1988)
36. D. Wildmann, S. Gnepf, F.K. Kneubühl: *Appl. Phys.* B **42**, 129–145 (1987)
37. J. Arnesson, S. Gnepf, F.K. Kneubühl: *First Detection of Higher Modes of a Helical Feedback (HFB) Gas Laser*, AIP Conf. Proc. No. 146, 1st Int. Laser Science Conf., Dallas, TX, USA, 149–150 (1986)
38. J. Arnesson, S. Gnepf, F.K. Kneubühl: *Helical Feedback (HFB) Gas Laser*, Digest 11th Int. Conf. Infrared and mmWaves, Tirrenia-Pisa, I, 542–544 (1986)
39. L.S. Goldberg, J.M. Schnur: *Tunable Internal-Feedback Liquid Crystal-Dye Laser*, US Patent 3,771,065 (9.8.72), CA80, 21324a (1974)
40. F.K. Kneubühl: *Infrared Physics* **23**, 115–117 (1983)
41. B.Z. Katsenelenbaum: *Theory of Irregular Waveguides with Slowly Changing Parameters*, Izd. Akad. Nauk. SSR, Moscow 1961 (in Russian), transl. in: FTD-ID(RS)T-0243-79, Foreign Technology Division WP.AFB, Ohio (1979)
42. N.F. Kovalev, I.M. Orlova, M.I. Petelin: *Sov. Phys.: Radio Phys. Quant. Electron.* **11**, 449–450 (1968)
43. A.H. Nayfeh, O.R. Asfar: *J. Appl. Phys.* **45**, 4797–4800 (1974)
44. O.R. Asfar, A.H. Nayfeh: *IEEE Trans. MTT*-**28**, 1187–1191 (1975)
45. M. Joindot: *Ann. Télécommun.* **31**, 281–290 (1976)
46. G.G. Denisov, M.G. Reznikov: *Sov. Phys.: Radio Phys. Quant. Electron.* **25**, 407–413 (1983)
47. V.L. Bratman, G.G. Denisov, N.S. Ginzburg, M.I. Petelin: *IEEE J. QE*-**19**, 282–296 (1983)
48. R.A. Schill, Jr., S.R. Seshadri: *Int. J. Infr. mmWaves* **7**, 1129–1167 (1986)
49. F.E. Borgnis, C.H. Papas: *Electromagnetic Waveguides and Resonators*, Encyclopedia of Physics, Vol. XVI, ed. by S. Flügge (Springer, Berlin 1958) pp. 285–442
50. N. Marcuwitz: *Waveguide Handbook* (McGraw-Hill, New York 1951)
51. K. Pöschl: *Mathematische Methoden in der Hochfrequenz-technik* (Springer, Berlin 1956)
52. L.A. Vainshtein: *Izd. Sov. Radio, Moscow* (in Russian) (1957)
53. H. Haken: *Light* (North-Holland, New York 1985)
54. V.A. Yakubovich, V.M. Starzhinskii: *Linear Differential Equations with Periodic Coefficients* (Wiley, New York 1975)
55. A.J. Palmer: *IEEE J. QE*-**23**, 65–70 (1987)
56. S.R. Chinn: *IEEE J. QE*-**9**, 574–580 (1973)
57. W. Streifer, R.D. Burnham, D.R. Scifres: *IEEE J. QE*-**11**, 154–161 (1975)
58. C.H. Henry: *IEEE J. QE*-**21**, 154–161 (1985)
59. S.L. McCall, P.M. Platzman: *IEEE J. QE*-**21**, 1899–1904 (1985)
60. D. Wildmann, S. Gnepf, F.K. Kneubühl: *Helv. Phys. Acta* **59**, 1053–1056 (1986)
61. H. Kogelnik: *Bell. Sys. Techn. J.* **55**, 109–122 (1976)
62. K.O. Hill, A. Watanabe: *Appl. Opt.* **14**, 950–961 (1975)
63. H.A. Haus: *Appl. Opt.* **14**, 2650–2652 (1975)
64. P. Szczepanski: *Appl. Opt.* **24**, 3574–3578 (1985)
65. K.O. Hill, R.I. MacDonald: *IEEE J. QE*-**12**, 716–721 (1976)
66. P. Szczepanski: *IEEE J. QE*-**22**, 517–519 (1986)
67. P. Szczepanski: *J. Appl. Phys.* **63**, 4854–4859 (1988)
68. D.T. Hodges, J.R. Tucker, T.S. Hartwick: *Infr. Phys.* **16**, 175–182 (1976)
69. Landoldt-Börnstein: *Zahlenwerte und Funktionen: Technik*, Bd. IV: 2b, 6. Aufl., ed. by H. Borchers and E. Schmidt (Springer, Berlin 1964)
70. *AIP Handbook*, 3rd edn. (McGraw-Hill, New York 1972)
71. D. Wildmann, R. Furler, H.P. Preiswerk, X. Zheng, F.K. Kneubühl: *Helv. Phys. Acta* **57**, 256–258 (1984)
72. D. Wildmann, X. Zheng, F.K. Kneubühl: *Int. J. Infr. mmWaves* **5**, 537–545 (1984)
73. A. Semet, S. Obenschein, N.C. Luhmann, Jr.: *Infr. Phys.* **16**, 189–191 (1976)